HHS Public Access

Author manuscript

Cell Rep. Author manuscript; available in PMC 2025 April 24.

Published in final edited form as:

Cell Rep. 2025 March 25; 44(3): 115408. doi:10.1016/j.celrep.2025.115408.

Podoplanin-positive cell-derived small extracellular vesicles contribute to cardiac amyloidosis after myocardial infarction

Maria Cimini[1], **Ulrich H.E. Hansmann**[2], **Carolina Gonzalez**[1], **Andrew D. Chesney**[2], **May M. Truongcao**[1], **Erhe Gao**[1], **Tao Wang**[1,3], **Rajika Roy**[4], **Elvira Forte**[5], **Vandana Mallaredy**[1], **Charan Thej**[1], **Ajit Magadum**[1], **Darukeshwara Joladarashi**[1], **Cindy Benedict**[1], **Water J. Koch**[4], **Çağla Tükel**[6], **Raj Kishore**[1,3,7,*]

[1]Aging and Cardiovascular Discovery Center, Lewis Katz School of Medicine, Temple University, Philadelphia, PA 19140, USA

[2]Department of Chemistry and Biochemistry, University of Oklahoma, Norman, OK 73019-5251, USA

[3]Department of Cardiovascular Sciences, Lewis Katz School of Medicine, Temple University, Philadelphia, PA 19140, USA

[4]Department of Surgery, Duke University School of Medicine, Durham, NC 27710, USA

[5]The Jackson Laboratory, Bar Harbor, ME, USA

[6]Center for Microbiology & Immunology, Lewis Katz School of Medicine, Temple University, Philadelphia, PA 19140, USA

[7]Lead contact

SUMMARY

Cardiac amyloidosis is a secondary phenomenon of an already pre-existing chronic condition. Whether cardiac amyloidosis represents one of the complications post myocardial infarction (MI) has yet to be fully understood. Here, we show that amyloidosis occurs after MI and that amyloid fibers are composed of macrophage-derived serum amyloid A 3 (SAA3) monomers. SAA3 overproduction in macrophages is triggered by exosomal communication from cardiac stromal cells (CSCs), which, in response to MI, activate the expression of a platelet aggregation-inducing

*Correspondence: raj.kishore@temple.edu.

AUTHOR CONTRIBUTIONS

M.C. conceptualized this study, designed and performed experiments, analyzed data, and wrote and revised the manuscript. U.H.E.H. designed and performed computational experiments and analyzed DRI-R5S data. C.G. performed experiments. A.D.C. performed computational experiments and analyzed DRI-R5S data. M.M.T. performed experiments. E.G. performed myocardial infarctions and conducted a blinded hemodynamic analysis. T.W. performed myocardial infarctions. R.R. conducted blinded echocardiography and analyzed the data. E.F. analyzed single-cell sequencing data. V.M. performed experiments. C.T. performed experiments. A.M. performed experiments. D.J. performed experiments. C.B. performed experiments. W.J.K. edited the manuscript. Ç.T. helped to conceptualize this study and its design. R.K. conceptualized the study, designed experiments, and finalized and approved the manuscript. All authors have given approval to the final version of the manuscript.

DECLARATION OF INTERESTS

The authors declare no competing interests.

SUPPLEMENTAL INFORMATION

Supplemental information can be found online at https://doi.org/10.1016/j.celrep.2025.115408.

type I transmembrane glycoprotein, Podoplanin (PDPN). CSC^{PDPN+}-derived small extracellular vesicles (sEVs) are enriched in SAA3, and exosomal SAA3 engages with macrophage by Toll-like receptor 2, triggering overproduction with consequent impaired clearance and aggregation of SAA3 monomers into rigid fibers. SAA3 amyloid deposits reduce cardiac contractility and increase scar stiffness. Inhibition of SAA3 aggregation by retro-inverso D-peptide, specifically designed to bind SAA3 monomers, prevents the deposition of SAA3 amyloid fibrils and improves heart function post MI.

In brief

Cumbersome serum amyloid A 3 (SAA3) structures accumulate in the heart after myocardial infarction, impairing left ventricle wall contractility. Cimini et al. report that exosomal SAA3 triggers SAA3 overproduction in macrophages after binding Toll-like receptor 2 and activating p38-MAPK phosphorylation. The retroinverso D-peptide DRI-R5S abrogates SAA3 monomer aggregation and amyloid formation.

Graphical Abstract

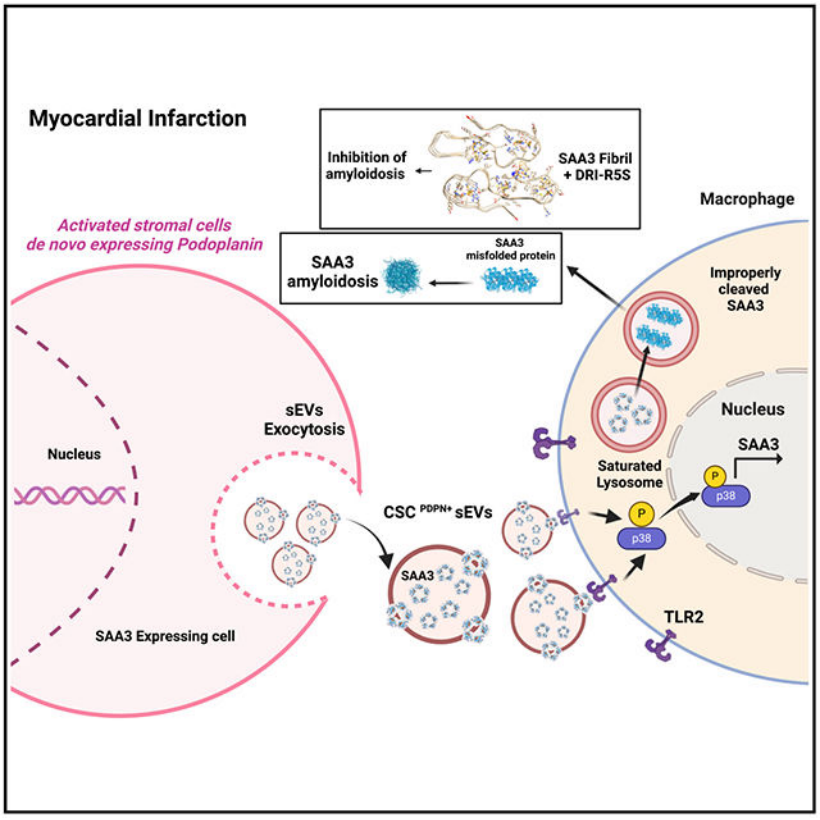

INTRODUCTION

Amyloidoses are a heterogeneous group of diseases characterized by the extracellular accumulation of stable and poorly soluble monomeric proteins that are turned into a pathological fibrillar form due to the overproduction of wild-type protein.[1] Rigid amyloid

fibrils are toxic and resistant to proteolytic degradation,[2,3] and their deposition leads to immune activation, destruction of tissues, and organ failure.[4] Frequently studied cardiac amyloidoses are caused by aggregation of immunoglobulin light chains, transthyretin, fibrinogen, and apolipoprotein in a healthy heart as a consequence of systemic chronic inflammation,[1] leading to tissue stiffness, congestive heart failure, and arrhythmias.[4,5] Chronic myocardial infarction (MI) is considered a systemic inflammatory condition, but whether amyloidosis can also occur after MI has yet to be fully understood.[6–16]

Possible deposition of rigid amyloid fibers after MI can reduce the remodeling of the ischemic area and enhance extracellular matrix (ECM) rigidity and stiffness, impairing the scar contribution to left ventricle function after MI.[17,18] Here, we document that amyloidosis occurs after MI and that amyloid fibers are composed of macrophage-derived serum amyloid A 3 (SAA3) monomers. SAA3 overproduction in macrophages is triggered by exosomal communication from a subset of activated cardiac stromal cells (CSC), which, in response to MI, *de novo* acquire the expression of a platelet aggregation-inducing type I transmembrane glycoprotein named Podoplanin (PDPN).[19–21]

PDPN acquisition enables CSCs to interact and communicate with recruited immune cells ($CD11b^{high}$), which express the PDPN receptor C-type lectin-like receptor 2 (CLEC-2).[22] Additionally, cardiac CSC^{PDPN+} communicate with macrophages by releasing small extracellular vesicles (sEVs). sEVs range from 30 to 150 nm in size, are considered major paracrine mediators of cell-to-cell communication,[23] and deliver beneficial or detrimental signals to neighboring and distant cells by exchanging their cargo, including protein, non-coding RNA, and lipid.[24,25] Existing literature suggests that the cellular microenvironment alters sEV content and function[26,27] and that, during myocardial injury and repair, sEVs actively participate in intercellular communication between different cell types.[28] Through proteomic analysis of CSC^{PDPN+}-derived sEVs (CSC^{PDPN+} sEVs), we identify SAA3 protein as an exclusively and highly enriched component of the exosomal cargo.[29]

SAA proteins are the major acute-phase plasma proteins that function in innate immunity and are the protein precursor of AA amyloidosis.[30–33] SAA1, SAA2, and SAA4 are circulating SAAs synthesized largely by hepatocytes[34–37]; SAA3 does not contribute to systemic SAA levels, is expressed extra-hepatically,[37] and exerts localized effects at the site of injury.[38] SAA3 binds to Toll-like receptor 2 (TLR2) on macrophages, initiating an autocrine communication to enhance the self-production of SAA3 and the expression of other cytokines and chemokines.[39,40] During chronic inflammation, the abundance of SAA3 derived from activated macrophages impairs SAA3 clearance, and saturated lysosomes release SAA3 monomers enriched in β sheets motifs that are prone to aggregate and accumulate into insoluble amyloid protofilaments in the ECM.[2,41–43] In the heart after MI, macrophages represent the most abundant cell population bearing TLR2 receptors; therefore, we investigated whether sEV-SAA3 triggers SAA3 synthesis in macrophages and whether SAA3 accumulates in ischemic hearts in amyloid fibers, hindering the contractility of viable myocardium and impairing organ function.[44,45]

We report that sEVs derived from CSC^{PDPN+} isolated from post-MI hearts and injected in normal uninjured mouse hearts lead to immune cell recruitment, fibrosis, cardiac

amyloidosis, and depressed cardiac function. CSC^{PDPN+} sEV-delivered SAA3 protein engages with TRL2 on macrophages, triggering an overproduction of SAA3 proteins, resulting in aggregation of SAA3 monomers as amyloid deposits in the extracellular space. Using SAA3- and TLR2-deficient mouse models, we demonstrate that SAA3 delivered by CSC^{PDPN+} sEVs has a local function in promoting post-MI amyloidosis. To inhibit SAA3 monomer aggregation, we specifically designed a retro-inverso (antisense) peptide made of D-amino acids (DRI) and showed that it effectively prevents amyloidosis[46] and improves post-MI cardiac structure and function. DRIs are small hydrophilic proteins that are enzymatically protected because they are synthesized with D-ammino acids and minimally immunogenic and exert specific binding only with the target protein with minimal off-target affinity,[47,48] making them excellent pharmacological candidates.[49–52]

RESULTS

CSC^{PDPN+} sEVs induce cardiac injury in healthy mouse hearts

The CSC^{PDPN+} cell population was identified and extensively characterized by our group using flow cytometry and immunohistochemistry analysis (Figure S1E) at different stages post MI. We found that, while co-expressed with PDGFRα, PDGFRβ, and CD34, PDPN was absent in fully differentiated (αSMA-positive myofibroblasts) (Figure S1E).[19–21] PDPN expression at the single-cell level after MI, derived using a publicly available published dataset, further confirmed our observations (Figure S1).[53] A single-cell RNA sequencing dataset comprising several time points post MI (sham and days 1, 3, 5, 7, 14, and 28) confirmed that PDPN is expressed in stromal cells only after injury and mostly in the activated epicardium and injury response fibroblasts characterized by the expression of pro-inflammatory genes such as Mt1 and Mt2 (Figure S1). We visualized PDPN expression through various plots: a FeaturePlot (Figure S1B), a violin plot (Figure S1C), and a dot plot (Figure S1D). Data indicated that PDPN expression is notably high in lymphatic endothelial cells and is also upregulated in activated stromal cells on day 1 post MI and in activated epicardium from days 3–28. Additionally, Forte et al.[53] showed the specific gene enrichment of all 11 fibroblast subclusters obtained with Seurat (PC20, resolution 0.5) from the stromal cell aggregate, and PDPN was specifically expressed only in ischemia-reperfusion conditions in epicardial and phagocytic fibroblasts/stromal cells. To study the sEV-mediated communication of CSC^{PDPN+}, we isolated CSC^{PDPN+} from mouse hearts 2 days after MI[20] (Figure S1F), expanded them in culture for 2–3 weeks, and isolated the sEVs from the conditioned medium.[28] Since CSCs in the heart acquire PDPN only after MI[19–21] (Figure S1), we verified whether the culture expansion without any stimuli maintains PDPN expression as a marker of stromal cell activation, akin to post-MI hearts. PDPN expression was diminished by the cells in culture (Figure S1G). To maintain the activated cell status during culture expansion, cells were treated with tumor necrosis factor alpha (TNF-α) (50 ng/mL) and Angiotensin II (AngII; 50 nM/mL), two abundantly expressed inflammatory and neurohormonal molecules in ischemic hearts that trigger PDPN expression and do not initiate cell differentiation,[54–60] and sEVs were isolated from the conditioned medium as per our published studies.[26,28,61] sEVs derived from similarly treated mouse cardiac lymphatic endothelial cells (mLECs), which physiologically express PDPN, and mouse cardiac endothelial cells (mCECs), which do not express PDPN, were used

as a control to exclude specific effects of PDPN expression and *in vitro* TNF-α/AngII treatment. In this study, CSC^{PDPN+} sEVs, mLECs sEVs, and mCECs sEVs are sEVs isolated from CSC^{PDPN+}, mLECs, or mCECs, respectively, treated with TNF-α and AngII unless otherwise specified. CSC^{PDPN+} sEVs were analyzed with a nanoparticle tracking analysis (Nanosight) to verify size (100–150 nm) and concentration (Figure 2A) and with expression of sEV marker proteins (Figure 2B). Additionally, sEVs were characterized by transmission electron microscopy (Figure 2C). To understand the effects of the paracrine signals of CSC^{PDPN+} via their sEVs, 2.5×10^8 sEV isolated from CSC^{PDPN+}, mLECs, or mCECs were injected into the left ventricle of healthy 10- to 12-week-old C57BL/6J mouse hearts, followed by weekly booster doses of same particle numbers by retro-orbital injections[62] (Figure S2A). Mice injected with saline were used as a further control. Echocardiography was performed at the baseline and 30 days after initial treatments to observe the effect of sEV treatments on heart physiology (Figure 1A). Mice injected with CSC^{PDPN+} sEVs or mLECs sEVs showed a reduction in the percent ejection fraction (%EF) (Figure 1A) and percent fractional shortening (%FS) (Figure 1A) with an increase in the end-systolic (Figure 1A) and -diastolic (Figure 1A) volumes (ESV and EDV, respectively), suggesting repression of cardiac function. Histological analysis showed epicardial and infiltrative fibrosis in animals treated with CSC^{PDPN+} sEVs and mLECs sEVs (Figure 1B; quantified in Figure 1C), which was not observed in the animals treated with mCEC-derived sEvs (Figures 1B and 1C). The fibrotic tissue in CSC^{PDPN+} sEV- and mLEC sEV-treated hearts was characterized by extensive infiltration of $CD45^+$ immune cells (Figure 1D; quantified in Figure 1E), which was not observed in the group treated with mCEC-derived sEVs (Figure 1D; quantified in Figure 1E). These *in vivo* studies suggest that, during ischemic conditions, CSC and mLEC intracellular communication enhances scar formation, ECM deposition, and immune cell recruitment.

Amylogenic SAA3 protein represents the signature component of CSC^{PDPN+} sEvs

We performed proteomics analysis using mass spectrometry on sEVs derived from untreated or TNF-α/AngII-treated CSC^{PDPN+} and mLECs (Figure S2B). Since mLECs physiologically express PDPN, we determined whether protein cargo in the sEVs differs between mLECsconstitutively expressing PDPN and CSC^{PDPN+} activating PDPN expression *de novo* in response to MI. mLECs were isolated from normal mouse hearts and either stimulated or not with TNF-α/AngII. CSC^{PDPN+} and mLECs shared ~1,000 proteins in the sEV cargo (Figure 2E), and CSC^{PDPN+} were distinctively enriched in ~2,000 proteins (Figure 2E). Within the exclusive proteins present only in the CSC^{PDPN+} sEVs, expression of ~1,200 was significantly changed after TNF-α/AngII treatment (Figure 2F). Only a few proteins were specifically present either in the untreated or TNF-α/AngII-treated group (Figure S2C). Comparative protein analysis among exclusively expressed proteins in CSC^{PDPN+} sEVs groups showed that SAA3 was quantitatively and statistically upregulated in CSC^{PDPN+} sEVs from cells stimulated with TNF-α/AngII (Figure 2F). To exclude the effects of TNF-α/AngII stimulation, we similarly treated mCECs that did not express PDPN and evaluated the impact of the stimulation on SAA3 synthesis. mCECs minimally expressed SAA3 in cells after the stimulus (Figure 2H). Similarly stimulated CSC^{PDPN+} isolated from global SAA3 knockout (KO) mice[63] (Figure S2H) were used as a further negative control and did not express SAA3 after treatment (Figure 2H). We confirmed by

western blots analysis that SAA3 was exclusively present in sEVs isolated from pretreated CSC^{PDPN+} and was undetectable in sEvs derived from similarly stimulated mLECs, mCECs, and SAA3 KO CSC^{PDPN+} (Figure 2G), suggesting that cells naturally expressing PDPN and expressing PDPN *de novo* have a distinct protein profile and that the sole expression of PDPN is not a prerequisite for SAA3 expression. Moreover, SAA3 expression in CSC^{PDPN+} sEVs is cell specific and not a consequence of *in vitro* TNF-α/AngII stimulation, and *de novo* PDPN expression is a prerequisite for SAA3 expression by CSCs. Gene Ontology analysis of the biological processes (Figure S2D), cellular components (Figure S2E), molecular functions (Figure S2F), and pathways activation (Figure S2G) suggested that the sEV proteins were associated with ECM modulation, and proteins associated with sEV formation indicated that our samples were specifically sEVs (Figure S2E).[64] Since LEC-derived sEVs are not carriers of SAA3, they were not used for further experiments.

sEV-SAA3 is essential to initiate a pathological response *in vivo*

To evaluate the importance and contribution of sEV-SAA3 in the paracrine communication of CSC^{PDPN+}, we injected into healthy mouse hearts CSC^{PDPN+} sEVs derived from CSC^{PDPN+} isolated from SAA3 KO mice[63] (Figure 3A). CSC^{PDPN+} from SAA3 KO mouse hearts 2 days after MI were isolated and stimulated exactly like wild-type CSC^{PDPN+} before isolation of sEVs from the conditioned medium (Figure 3A). SAA3 KO-CSC^{PDPN+} sEVs did not show any differences in cardiac functions (Figure 3B), and histologically, SAA3 KO-CSC^{PDPN+}-derived sEVs induced minimal interstitial fibrosis (Figure 3C, right; quantified in Figure 3D) when compared with healthy mouse hearts injected with wild-type CSC^{PDPN+} sEVs (Figure 3C, left; quantified in Figure 3D). These data provide evidence that CSC^{PDPN+}-derived exosomal SAA3 contributes to the observed fibrotic responses and depressed cardiac function seen during the injections of wild-type CSC^{PDPN+} EVs.

sEV-SAA3 and TLR2 are necessary to trigger SAA3 overproduction in macrophages

SAA3 signals through TLR2 and SAA3 can initiate its own over-production.[39,40] Thus, we hypothesized that sEV-SAA3 binds TLR2 on macrophages, leading to the activation of downstream pathways and triggering an overproduction of SAA3.[65] To test this, we isolated bone marrow-derived macrophages (BMDMs) from wild-type and global TLR2 KO[66,67] mice, as described previously in our publication[20] (Figure S2I). We first verified whether the CSC^{PDPN+} sEV communication rather than the free protein-paracrine one is the major responsible for macrophage activation. We cultured wild-type BMDMs (~250,000) with conditioned medium derived from CSC^{PDPN+} depleted of the sEVs for 24 h and compared the expression of SAA3 and the major proinflammatory cytokines with BMDMs exposed to the CSC^{PDPN+}-derived sEVs (1×10^5/mL sEV particles) (Figure 4A). As shown, sEV-depleted CSC^{PDPN+} conditioned medium failed to activate the BMDMs when compared with BMDMs treated with CSC^{PDPN+} sEVs. *In vivo*, inhibition of sEV release would have not specifically inhibited CSC^{PDPN+} sEVs but, rather, from all cells, thereby confounding the specificity. We have recently published that systemic sEV inhibition by a powerful exosome inhibitor, tipifarnib, improves cardiac function and fibrosis in the heart failure model.[68] To further corroborate our data, wild-type BMDMs (~250,000) were treated with either 1×10^5/mL sEV particles of CSC^{PDPN+} or 10 μg of rSAA3 (Figure 2D). Lipopolysaccharides (LPS) (10 ng) and mCECs sEVs (1×10^5/mL) were used as controls.

1×10^5/mL sEV particles of CSC^{PDPN+} or 10 μg of rSAA3 stimulated the migration of wild-type BMDMs from the inner to the apical site of a Transwell insert (Figure S2J)[69] and activated them toward the pro-inflammatory phenotype, increasing the expression of the proinflammatory cytokines TNF-α and interleukin-1β as well as iNOS2 (Figures S3A and S3B) and a wide array of cytokines (Figures S3C and S3E) and chemokines (Figures S3D and S3F), usually released during the innate immunity inflammatory response.[69,70] On the contrary, either CSC^{PDPN+} sEVs or rSAA3 failed to activate TLR2 KO BMDMs (Figures S3A–S3F). Similarly, sEVs derived from SAA3-KO-CSC^{PDPN+} did not trigger the synthesis of inflammatory mediators in wild-type BMDMs (Figures S3A, S3C, and S3D). After verifying that CSC^{PDPN+} sEVs and rSAA3 can initiate a pro-inflammatory phenotype in BMDMs, we assessed whether they also triggered SAA3 expression (Figure S2I). Wild-type and TLR2 KO BMDMs were either treated with CSC^{PDPN+} sEVs, mCECs sEVs, SAA3 KO-CSC^{PDPN+} sEVs, or 10 μg of rSAA3 for 24 h. q-PCR, western blot, and ELISA analysis clearly showed that only wild-type BMDMs were able to express SAA3 (Figures 4B, left and right blots; 4C; and 4D) exclusively after treatment with CSC^{PDPN+} sEVs or rSAA3. sEVs derived from SAA3-KO CSC^{PDPN+} failed to activate TLR2-mediated SAA3 synthesis (Figures 4B, left and right blots; 4C; and 4D). These data show that SAA3 present in CSC^{PDPN+} sEVs initiates a self-release of SAA3 in macrophages only after binding to TLR2 and that TLR2 is required for SAA3 transcription.[71] Moreover, SAA3 is the required protein present in the CSC^{PDPN+} sEV cargo that can initiate SAA3 release in competent macrophages. Additionally, we isolated macrophages from cardiac tissue 3 days after MI from wild-type and SAA3 KO mice. Sham-operated animals were used as a control source of cardiac macrophages. We cultured the macrophages using the same conditions as for the BMDMs to evaluate the SAA3 expression from these 3 experimental groups. As shown in Figure S2K, cardiac macrophages isolated from wild-type hearts 3 days after MI showed increased expression of SAA3 compared to cardiac macrophages isolated from sham-operated mice or cardiac macrophages isolated from SAA3 KO animals. Therefore, this suggests that cardiac macrophages participate in SAA3 amyloid formation. To further corroborate our findings and to dissect the mechanism behind SAA3 synthesis, we verified that the signaling effectors of the TLR2 pathway were activated solely upon binding of rSAA3 with TLR2. Wild-type BMDMs were treated *in vitro* with 10 μg of rSAA3, and the classical kinases downstream of the TLR2 pathway were analyzed. We did not observe any differences in nuclear factor κB (NF-κB) or JNK phosphorylation after 15 min of treatment, since they are constitutively phosphorylated when monocytes become macrophages; however, treatment with rSAA3 rapidly activated the p38-mitogen-activated protein kinase (MAPK) pathway, inducing p38 phosphorylation (T180/Y182) (Figure 4E, quantification on the right).[39,63] LPS was used as a positive control (Figure S3G, quantification on the right). We further tested whether SAA3 present in CSC^{PDPN+} sEVs may independently activate p38 MAPK. We treated BMDMs with CSC^{PDPN+} sEVs and control sEVs. As shown in Figure 4F, 15 min of treatment with CSC^{PDPN+} sEVs resulted in higher p38-MAPK phosphorylation compared with baseline untreated wild-type BMDMs, which was not observed upon treatment with either mCECs sEVs or SAA3 KO-CSC^{PDPN+} sEVs (Figure 4F, quantification on the right). CSC^{PDPN+} sEV treatment, like rSAA3, did not generate differences in the phosphorylation of NF-κB or JNK (data not shown). These data suggested that SAA3 in CSC^{PDPN+} sEVs engages the p38-MAPK signaling pathway upon

binding to TLR2. Moreover, treatment of BMDMs with 20 μM of a p38-MAPK inhibitor, the SB 203580 compound, decreased SAA3 transcription (Figure 4G) and protein synthesis (Figure 4H, quantification on the right) along with diminished TNF-α, IL-1β, and iNOS2 expression (Figure S3I) after treatment with rSAA3. LPS was used as a control (Figure S3K, quantification on the right). These data show that sEV SAA3 triggers SAA3 expression in BMDMs upon binding with TLR2 and engaging in p38-MAPK phosphorylation.

CSC^{PDPN+} sEvs initiate SAA3 amyloidosis in healthy mouse hearts

Besides its function during inflammation, SAA3 can be the protein precursor of AA amyloidosis.[44] Based on the literature regarding amyloidosis after MI,[6–15] we verified the presence of amyloid fibers in the scar area of mouse hearts after ischemia with thioflavin S and Congo red staining, two gold-standard diagnostic approaches for amyloidosis.[4,72–74] Thioflavin S and Congo red molecules are specific dyes bound by amyloid fibrils, and amyloid deposits bound to Congo red molecules show characteristic birefringence when viewed with a polarizing microscope,[4,72–74] showing a golden color effect that is required for histological diagnosis.[74] Mouse hearts 30 days after MI showed positivity for thioflavin S fluorescence (Figure 5A, left) and Congo red birefringence (Figures 5B, left, and S4A, left and magnification in the middle) in the ischemic scar tissue (ischemic scar tissue labeled with Masson's trichrome staining in Figure S4B), confirming the elevated concentration of amyloid assemblies in the cardiac scar. Further, by micro-dissecting and separating the infarcted and border zone areas from the remote area, we confirmed that SAA3 was expressed in the ischemic area of mouse hearts after MI. The peak of macrophage migration after MI is between days 3 and 5; therefore, day 7 post MI represents a peak for SAA3 expression in the forming scar (Figure S4C). We also corroborated the histochemistry data with a specific western blot analysis of SAA3 deposition in the ischemic area of infarcted mouse hearts 30 days after MI (Figure S4D, quantification on the right). Furthermore, we validated via immunohistochemistry that SAA, labeled in green (Figures 5C, left, and 5D, left), aggregates in ischemic tissue of mouse hearts 30 days after MI along with ECM proteins, labeled with fibronectin in red (Figure 5C, left). More interestingly, healthy mouse hearts without any MI insult, injected with sEVs isolated from TNF-α/AngII-treated CSC^{PDPN+}, showed SAA amyloidosis 30 days after injection (Figures 5A–5C, center; 5B, magnification on the right; and S4E, left). Amyloid deposits were found in the fibrotic epicardial area (Figures 5A–5C, center; 5B, magnification on the right; and S4E, left), and Congo red stain showed specific birefringence when observed with polarized light (Figure 5B, center and magnification on the right). Healthy mouse hearts injected with mCECs sEVs did not develop any epicardial amyloidosis (Figures 5A, right, and S4E, center). Notably, deposition of SAA was not increased in mouse hearts injected with SAA3-null CSC^{PDPN+} sEVs (Figures 5C, right, and S4E, right), and SAA deposits were not observed in the fibrotic tissue or at the site of injection except weak deposition around capillaries (Figure 5C, right). These data showed that amyloidosis takes place after MI and that released SAA3 proteins can aggregate in amyloid deposits. Therefore, sEV SAA3, after triggering SAA3 overproduction via TLR2 in macrophages, represents a potential mechanism of SAA3-mediated cardiac amyloidosis. SAA amyloidosis has never been described in human hearts after ischemic injuries or during fibrotic tissue formation in heart failure.[6] We have shown previously that the cardiac fibrotic tissue of individuals with heart failure is populated

by CSC^{PDPN+}.[20] We therefore verified the presence of SAA amyloid deposits in human failing heart tissue. As expected, infiltrating fibrotic tissue of human heart samples derived from explanted hearts from patients with heart failure (Figure S4F) also contained extensive SAA amyloid deposits (labeled in green, Figures 5E and S4G). Taken together, these findings show that sEVs derived from pre-treated mCECs or SAA3-KO CSC^{PDPN+} fail to induce SAA3 amyloidosis in healthy mouse hearts and that SAA amyloidosis can also develop in humans.

SAA3 antisense D-peptide treatment reduces SAA3 oligomerization and amyloidosis after MI

Overproduction of SAA3 impairs SAA3 clearance, and lysosomes release dysfunctional SAA3 monomers that are prone to aggregate to insoluble amyloid protofilaments.[2,51] We measured the aggregation capacity with a protein aggregation assay to validate whether SAA3 monomers released by activated BMDMs are prone to aggregate in amyloid structure and thereby initiate amyloidosis. A protein aggregation assay[75] using thioflavin T showed that, after treatment with CSC^{PDPN+} sEVs (Figures S5A and S5B) or rSAA3 (Figures S5A and 5B) BMDM conditioned medium is enriched with insoluble amyloid structures that bind thioflavin T. These data further validated the idea that CSC^{PDPN+} sEVs and rSAA3 propel a SAA3 feedforward loop in BMDMs and that SAA3 levels are consistently elevated in BMDM conditioned medium after rSAA3 or CSC^{PDPN+} sEV treatments. Moreover, the presence of SAA3 amyloidosis after MI or injection of CSC^{PDPN+} sEVs in healthy mouse hearts compelled us to examine whether we can modulate the aggregation of SAA3 protofilaments *in vitro* and reduce post-MI amyloidosis *in vivo*. Interestingly, therapeutic approaches targeting a sterile innate immunity response have not yet succeeded because impaired inflammatory cell recruitment or neutralization of signature inflammatory cytokines negatively affects the scar formation and healing of the ischemic heart.[20,76] Building on a computational study,[46] we tested DRI-R5S (sequence: D-SFFSR),[46] an inhibitory peptide that acts as an antisense of the SAA3 binding sites and reduces the aggregation of amyloid fibrils without interfering with the inflammatory response (Figure 6A). The simulations of Jana et al.,[46] showed that the D-peptide interaction with SAA1-3 monomers made it more difficult for the β sheet chains to converge into the conformation taken in fibrils. They further showed that DRI-R5S strongly reduced the stability of SAA1 fibrils, which makes SAA fibril growth more difficult (Figure S5D). Taking advantage of what has been published on D-peptides as drug candidates[77] to reduce amyloidosis in Alzheimer's disease,[78–84] we treated BMDMs with 1×10^5/mL CSC^{PDPN+} sEVs along with different doses of DRI-R5S for 24 h. We measured the amyloid structures in the conditioned medium with a thioflavin T assay (Figure S5B). 25 μg of DRI-R5S was able to significantly reduce aggregation significantly. To further validate the activity of DRI-R5S, we treated BMDMs with rSAA3 and 25 μg of DRI-R5S for 24 h (Figure 6B). DRI-R5S treatment significantly reduced the aggregation activity of amyloid proteins after rSAA3 treatment (Figure 6B). Of note, docking analysis of DRI-R5S with fibronectin (Figure S5E) and collagen Iα (Figure S5F) proteins showed an affinity for fibronectin and collagen fibrotic structures, signifying that DRI-R5S prevents further interaction of SAA fibrils with ECM proteins. In light of these *in vitro* results, we treated wild-type animals with 100 nmol/kg of DRI-R5S delivered intraperitoneally every other day for

30 days after the induction of MI (Figure S5G). Untreated animals injected only with DRI-R5S vehicle (saline) were used as a control. By western blot (Figure 6C; quantified in Figure 6D) and immunohistochemistry (Figure 6E) analysis, we observed a significant reduction of SAA3 and SAA proteins in the scar tissues of mouse hearts treated with DRI-R5S for 30 days after MI surgery. Western blot analysis of the microdissected scar area from the rest of the heart of untreated control animals (Figure 6C; quantified in Figure 6D) showed an increased presence of SAA3 when compared with sham-operated mice. Reduced accumulation of SAA3 in the ECM contributed to better left ventricle function after ischemia (Figure 7A). Ischemic left ventricles of animals treated with DRI-R5S also showed significant scar reduction (Figure 7C) and viable myocardium composition (Figure 7B, magnification) when compared with the ischemic area of untreated animals (Figure 7B, magnification). The presence of viable cardiomyocytes and possible reduction in scar rigidity and stiffness likely improved the symptoms of the primary ischemia and reduced scar size. We performed MI in TLR2 global KO and SAA3 global KO animals to validate our findings and proposed mechanism in wild-type animals (Figure S6).[85] Wild-type animals injected with saline were used for comparison. After 30 days of MI, both TLR2 and SAA3 KO mice showed improved heart function, as shown by echocardiographic data[5] (Figure S6A), reduced scar size (Figure S6C; quantified in Figure S6D), and increased heart weight/body weight ratio (Figure S6E). The ischemic left ventricle wall of KO animals was also characterized by viable myocardium and, importantly, reduction of SAA in the ECM of TLR2 KO animals (Figure S7A; quantified in Figure S7C). Overall, ischemic tissue of both KO mice and wildtype mice treated with DRI-R5S showed improved vascularization 30 days after MI compared to wild-type untreated animals (Figure S7B; quantified in Figure S6D). Functional echocardiographic data were further validated with strain analysis. Strain analysis, the gold-standard technique to measure tissue elasticity,[17] did not show any differences between the percentage of radial strain in baseline and 30 days after MI in wild-type mouse hearts treated with DRI-R5S (Figure S6B). This finding indicated improved synchronous myocardial deformation indicative of improved left ventricular elasticity and, hence, improved left ventricular contractility and stretchiness of the scar tissue (Figure 7B, right). On the opposite, wild-type animals with MI and without any treatment showed a statistical reduction in the percentage of radial strain (Figure S6B), indicating scar stiffness. Both groups of animals at baseline showed a similar percentage of radial strain (16.9% and 17.7%). Our findings show that inhibiting SAA3 deposition reduced amyloidosis after MI and improved cardiac function, reversing scar formation.

DISCUSSION

In this study, we describe that amyloidosis can take place in the cardiac scar after MI and that it is mainly caused by aggregation of SAA3. SAA3 aggregation is a consequence of exacerbated macrophage activation by CSC^{PDPN+} sEVs. This mechanism presupposes the binding of exosomal SAA3 with TLR2 and activation of the TLR2 pathway with final phosphorylation of p38. To bypass this process, we directly interfered with amyloid fiber formation using a retro-inverso D-peptide, DRI-R5S, that binds SAA3 on self-aggregating sites. Our study revealed that DRI-R5S is a powerful pharmacological tool that impairs the

onset of amyloidosis during scar formation after ischemia and improves post-MI cardiac functions.

PDPN, a possible mesenchymal stromal cells inflammatory marker

Cardiac homeostasis is maintained through well-organized interaction between parenchymal cardiomyocytes and multiple other cell types.[86–89] CSCs play a distinct role in supporting cardiac growth and structure and in the maintenance of overall tissue homeostasis.[90] After MI, the tissue homeostasis is altered, and the physiological adaptation to a pathological condition consists of activating the highly specialized response cells of wound healing, including immune cells.[91–93] Among all specialized cells, CSCs *de novo* acquire a glycoprotein named PDPN as a sign of activation after ischemia.[19,21,53,90] CSC^{PDPN+} appear at the site of injury as early as 2 days after injury and extensively populate the ischemic area and border infarct zone over time to represent the most abundant type of cells that compose the scar during the acute phase after ischemia (Figures S1C and S1D). Physiologically, in the healthy adult heart, CSC^{PDPN+} are rare, and PDPN expression is mainly restricted to LECs. During embryogenesis, PDPN is essential for epicardial tissue and lymphatic system formation.[94–99] In adult life, PDPN is expressed by fibroblastic reticular cells (FRCs) in lymph nodes and allows immune cells to adhere to LECs and FRCs to facilitate migration and antigen presentation.[100–102] After MI, PDPN acts as an inflammatory marker, and newly acquired PDPN by CSCs helps them to interact and communicate with recruited immune cells ($CD11b^{high}$), which express a PDPN receptor named CLEC-2.[22] The interaction between PDPN and CLEC-2 activates an inflammatory response in immune cells,[103,104] and we recently showed that blocking the interaction between CSC^{PDPN+} and macrophages improved cardiac function and scar composition after infarction.[20,103,104] PDPN acquisition by CSCs has been described in various pathologies, including cardiovascular diseases and a variety of solid tumors and neuropathologies and during the progression of autoimmune and infectious diseases (Table S1). Taking into consideration that cells are described and classified by their markers and that CSC^{PDPN+} characterizes many pathologies, we can conclude that PDPN can be recognized as an established mesenchymal cell marker, specifically expressed *de novo* during inflammation or pathological conditions. At the moment, there is no consensus on mesenchymal stromal cell inflammatory markers, and PDPN can be the first of many. In the context of heart failure, not much is known about CSC^{PDPN+}, and our studies can open a new research avenue in the study of cardiovascular disease and add important information about the role of CSCs in pathological conditions. The fact that PDPN expression in CSCs occurs during or after immune activation raises the possibility that it is a non-canonical but conserved phenomenon during innate immunity response, aiming to improve cell-to-cell or paracrine communication between CSC^{PDPN+} and immune cells, which trigger the production and release of proinflammatory cytokines and chemokines, including SAA3.

Innate immunity and cardiac amyloidosis

SAA3 is a powerful pro-inflammatory enhancer of macrophage activation and recruitment (via TLR4), lymphocyte T helper differentiation in $Th\text{-}17^{+}$, and secondary SAA3 amyloidosis.[38–40,63,69] We show that SAA3 aggregates in amyloid structures in the scar after ischemia in murine and human hearts. Cardiac amyloidosis is an extensively studied field;

prominently investigated cardiac amyloidoses are secondary and caused by aggregation of immunoglobulin light chains, transthyretin, fibrinogen, and apolipoprotein in a healthy heart as a consequence of systemic inflammation.[1,2,4,30,51] Once these proteins create amyloid structures in the heart, the cardiac physiology declines, and the heart goes into failure. However, studies regarding amyloidosis after ischemia, mechanisms behind amyloid fibril accumulation, or which type of amyloid protein may aggregate after MI have yet to be reported. The fact that cardiac amyloidosis occurs as a secondary phenomenon of an already pre-existing chronic condition does not exclude the possibility that it can also occur after prolonged myocardial ischemia (chronic MI) or any other types of heart failure, which are considered chronic inflammatory conditionsl.[6,7,105] Our study not only reports the presence of amyloid proteins in human and murine failing hearts but also associates the onset of SAA3 amyloidosis with alternative intracellular communication between macrophages and CSC^{PDPN+}. Previous studies of chronic cardiovascular diseases have shown correlations between plasma levels of hepatic isoforms of SAA (SAA1 and SAA2) and death. Patients with MI or elevated ST and a high plasma level of SAA1-2 have a higher possibility of dying.[6–15] Causes of death after high plasma levels of SAA1-2 are unknown. SAA1-2 can accumulate in a healthy heart as a secondary amyloid structure; however, there are no reports on whether plasma SAA1-2 also aggregate in the ischemic scar after MI in addition to locally released SAA3. SAA3 is an inflammatory protein that is very conserved and described as one of the major 25 inflammatory markers in a variety of diseases.[92] This manuscript specifically reports sEV SAA3 binding to macrophage TLR2, leading to overproduction and release of SAA3. A literature review of pathological conditions characterized by SAA3 overexpression, deposition as amyloidosis, and acquisition by mesenchymal stromal or other cell types can be found in Table S2. The types of pathologies in which SAA3 amyloidosis is present and SAA3 is the dominant cytokine unexpectedly result in diseases similar to those in which PDPN is acquired *de novo* by CSCs (Table S1). Thus, there may be a correlation between PDPN acquisition by CSCs and SAA3 overexpression and consequent amyloidosis. SAA3 and PDPN are new critical players during inflammation but are involved in mechanisms that cannot be abrogated or inhibited. Blocking TLR2 or interfering with innate immunity activation has been shown in many clinical trials to be detrimental rather than helpful. Thus, we approached the problem using an alternative system that does not interfere with the innate immunity response and is currently under investigation for the treatment of protein-aggregating diseases like Alzheimer's disease.

DRI as a pharmacological tool

Retro-inverso D-peptides are attractive tools with excellent pharmacokinetics, pharmacodynamics, and few off-target effects. These small peptides specifically bind the sequence for which they were designed, and unless they were created to block the interaction between ligands and receptors, they do not interfere with paracrine communications.[47–49] We took advantage of these characteristics and developed a D-peptide, DRI-R5S, to inhibit SAA3 aggregation,[46] resulting in efficiency and specificity.[106,107] Our peptide does not interfere with the binding of TLR2 with SAA3 or with any other pathway involved in innate immunity; thus, innate immune reaction and inflammation were not inhibited during our treatment.[76] This is fundamental for proper scar

formation. Therapies with retro-inverso D-peptides, to our knowledge, have been proposed in the past for the treatment of Alzheimer's disease, but the design or the employment of D-peptides for the treatment of cardiovascular disease has never been done before. Our data showing that a retro-inverso D-peptide inhibits protein aggregation after MI suggest that these peptides are safe tools to enhance scar reversal without engaging in regeneration mechanisms. Our results confirmed that inhibiting the aggregation of cumbersome structures without blocking any physiological reaction is not only propaedeutic for healthy scar formation, but the treatment is safe and restricted to the timing of macrophage activation and resolution of inflammation. Treatments with D-peptides may be beneficial for the treatment of all diseases characterized by SAA3 overexpression/amyloidosis; for example, to avoid the growth of atherosclerotic plaques or to inhibit the aggregation of other kinds of amyloid proteins, since currently there are no specific treatments for cardiac amyloidosis.

Limitations of the study

SAA3 overproduction by other immune cells bearing TLR2, like dendritic cells, has not yet been investigated, nor has the generation of an inducible PDPN-specific SAA3 KO mouse. A comprehensive investigation of SAA3 amyloidosis formation encompassing a larger cohort of immune cells using a transgenic mouse model is needed to establish the functional role of CSC^{PDPN+} in the innate immunity response.

Conclusion

SAA3 amyloidosis occurs after MI and further impairs ischemic heart function. We developed a safe tool that does not inhibit or interfere with the communication between CSCs and macrophages but can indirectly modulate the exacerbation of scar formation post MI, abrogating the onset of SAA3 amyloidosis. Besides MI and heart failure, many pathologies characterized by CSC^{PDPN+} and SAA3 amyloidosis could benefit from our findings. Moreover, this new treatment may work alongside existing therapies.

RESOURCE AVAILABILITY

Lead contact

Requests for further information, resources, and reagents should be directed to and will be fulfilled by the lead contact, Dr. Raj Kishore (raj.kishore@temple.edu).

Materials availability

New unique materials were not generated in the course of this study.

Data and code availability

The mass spectrometry proteomics data have been deposited to the ProteomeXchange Consortium via the MassIVE partner repository with the dataset identifier MSV000097049 and are publicly available as of the date of publication. This paper does not report original code. Additional information required to reanalyze the data reported in this paper is available from the lead contact upon request. Single-cell-RNA sequencing data are publicly

available at the Array Express repository. The accession number for these data is listed in the key resources table

STAR★METHODS

EXPERIMENTAL MODEL AND STUDY PARTICIPANT DETAILS

Animals—All animal experiments were conducted according to the NIH Guide for the Care and Use of Laboratory Animals and were approved by the Institutional Animal Care and Use Committee (IACUC) of Temple University. Ten- to 12-weeks-old male and female wild type (WT) (C57BL/6J), male and female global Toll Like Receptor 2 knockout (TLR2KO; Jackson Labs; Tlr2tm1Kir/J)[66,67] and male and female global Serum Amyloid A3 (SAA3) (Jackson Labs; Del(7Saa3-Saa2)738Lvh/J)[63,108] knockout mice (SAA3 KO) were purchased from Jackson Research Laboratory (Bar Harbor, ME). We used both the sexes in our study to account for potential sex-based biological differences, as variations in physiology, metabolism, and treatment responses have been documented. This approach helps in producing more reliable and generalizable results, enhancing the validity of our findings.

Human heart tissues samples—De-identified Heart tissue samples (n = 5) obtained from heart failure patients at the time of transplantation and were stored at tissue biobank at the Lewis Katz school of Medicine, Temple University, Philadelphia, Pennsylvania and immediately frozen in liquid nitrogen and stored at −80°C until use. The study was conducted in accordance with the Declaration of Helsinki. All tissues collection was done following protocol approved by the Temple University Institutional Review Board.

Cell lines—Mouse cardiac endothelial cells (mCECs) were purchased and validated from Cedarlane research Products and was cultured expanded. The cell line was periodically tested and was negative for mycoplasma.

Primary cell cultures—Infarcted WT and SAA3 KO mice were euthanized two days after MI surgery, as described above. The hearts were excised and extensively washed in phosphate-buffered saline. The cardiac tissues were minced and subjected to repetitive rounds of enzymatic digestion with collagenase type 2 (Worthington Biochemical Corp.) until complete dissociation. Larger cells, such as mature myocytes, were precipitated (centrifuged at 100g for 1 minute), and the supernatants containing small cell populations were filtered through 40 μm cell strainers. For positive cell separation, the small cell population was incubated with a biotinylated Podoplanin antibody (table) previously bound with magnetic beads (Milteniy) for 20 minutes at 4C. Cells were sorted through magnetic cell separation columns (Milteniy). After washing, the cells were cultured in an expansion medium on collagen-coated flasks. The purity of the isolation was analyzed by flow cytometry for Podoplanin, LYVE-1 and CD68 on detached (0.2% trypsin) and fixed (4% PFA) cultured CSC^{PDPN+} cells. Cardiac macrophages were isolated from the Podoplanin negative cells' fraction and cultured as described below for bone marrow (BM) derived macrophages. Lymphatic endothelial cells (mLECs) were isolated from WT uninjured mouse hearts with the same methodology. mCECs purchased from Cedarlane were cultured

expanded. After expansion, all types of cells were cultured in media supplemented with sEVs-free FBS and treated with 50ng/mL of TNFα (R&D) and 50nM Angiotensin II (Sigma). Conditioned media was harvested every two days and combined to isolate cell-derived sEVs from the conditioned media (described below). BM-derived monocytes were isolated from WT and TLR2 KO BMs mononuclear cells of mice fore and limbs with density-gradient centrifugation as described previously.[20] Mononuclear cells were seeded on plastic dishes, and the medium was changed after 40 minutes. The monocyte population was cultured and derived in macrophages with 20% FBS, 1% Penicillin/Streptomycin solution, and 20% of L929 conditioned medium in RPMI medium as previously described. Bone marrow-derived macrophages (BMDM), when treated with CSC^{PDPN+} sEVs, were cultured with expansion media made with RPMI, 20% sEVs-free FBS, 1% Penicillin/Streptomycin and 10ng/mL monocyte colony-stimulating factor (Sigma). Wild-type BMDM (~250,000) were treated with either 10μg, 25μg, or 50μg of recombinant SAA3 (rSAA3) or $1x10^4$, $1x10^5$, $5x10^5$ particles /mL of CSC^{PDPN+} sEVs for 6, 12 and 24h (Figure S3A). q-PCR analysis for the TLR2 downstream signature cytokines was performed to evaluate the best time point and lowest dose of rSAA3 and exosomal particles needed to activate BMDM. Lipopolysaccharides (LPS) were used as a control (10ng/mL). The specific activation of BMDM via sEVs was established by measuring major cytokine and SAA3 expression after 24h of culture in CSC^{PDPN+} conditioned media depleted from sEVs or with CSC^{PDPN+} derived sEVs. For this experiment, we freshly isolated CSC^{PDPN+} from mouse hearts 2 days after MI and cultured them for 5 days, without further activation with TNFα and Angiotensin II. We isolated the conditioned media and depleted it from the sEVs. sEVs from this conditioned media were used in the experiment. The migratory activity of BMDM was evaluated with a transwell migration assay. BMDM were seeded on the inner side of transwell insets (Corning, 0.8 μm) and let migrated from basal to apical side of transwell insets in different conditions for 24h. BMDM migrated to the apical side were detached with 0.2% trypsin, and the absolute number of migrating cells was counted.

METHOD DETAILS

Animal surgeries—For physiological assessment and histological analyses, healthy and uninjured ten- to 12-weeks-old male wild type (WT) (C57BL/6J) mice were injected with $2.5x10^8$ small extracellular particles isolated from WT or SAA3 KO-CSC^{PDPN+} or murine cardiac lymphatic endothelial cells (mLECs) conditioned media or murine cardiac endothelial cells (mCECs) conditioned media or saline, in the left ventricle followed by weekly booster doses of same particle numbers by retro-orbital injections. Ten- to 12-week-old male WT, male and female TLR2 KO, and male and female SAA3 KO mice underwent MI surgery previously described in our papers.[20] Briefly, MI was induced through the permanent ligation of the left ventricular descending coronary artery (LAD). All animals were screened for baseline and post-MI echocardiography before MI and exosomal treatments and at 7 and 30 days after both treatments. Following MI, WT animals only were injected i.p. with 100 nmol/kg of DRI- $R5S^{14}$ peptide dissolved in saline once every other day for 30 days or peptide vehicle as a control (saline). At 3, 7, and 30 days after MI, animals were sacrificed under deep anesthesia, bilateral thoracotomy was performed, and the hearts were removed. Mouse hearts at 3, 7, and 30 days after MI were micro-dissected to isolate ischemic and border zone areas from the remote location and lysate in lysis buffer

(Cell Signaling Technology) or quiazol (Qiagen). Mouse hearts injected with sEVs were fixed in 4% paraformaldehyde (PFA) and embedded in OCT instead ischemic mouse hearts 30 days after MI were fixed in 10% Formalin (animals subjected to MI) and embedded in paraffin and processed for histological analysis (described below). Furthermore, WT and SAA3 KO mice were euthanized two days after MI, and heart samples were collected for cell culture, as described below.

Transthoracic echocardiographic analysis and strain—Echocardiography was performed using the Vevo 2100 imaging system from VisualSonics, as published.[20] Briefly, transthoracic two-dimensional echocardiography in mice anesthetized with 2% isoflurane was served with an 18-38 MHz probe. M-mode echocardiography was carried out in the parasternal long axis in mice to assess heart rate (HR), left ventricular (LV) internal diameter in diastole (LVIDd) and systole (LVIDs), LV anterior and posterior wall thickness in diastole and systole (LVAWd and LVAWs as well as LVPWd and LVAWs, respectively). LV fractional shortening (FS%), ejection fraction (EF%), and end-systolic and diastolic volumes were calculated (ESV and EDV).[20] Speckle tracking strain analysis was done using b-mode loops with a frame rate of 300 at a stable heart rate. M-mode and B-mode data were acquired at baseline and four weeks post-MI in all animals and groups. Global strain and strain rate were analyzed at baseline and post-MI. For all strain analyses, endocardial deformations of the left ventricle were analyzed. All m-mode data analysis was performed using VevoLAB 5.8.1 software, and strain analyses were performed using the Vevo Strain function of Vevo LAB software. All data acquisition and analysis were done blinded.

Histological assessments and immunohistochemistry of thin cardiac sections —After harvest, either mouse or human hearts were washed with phosphate-buffered saline (PBS), fixed at least for 48h with 4% PFA or 10% formalin, and embedded in OCT (PFA fixed-sucrose gradient) or paraffin (formalin fixed-ethanol and xylene gradient). Cardiac tissues were cut into 5-4 μm-thick sections. Following PBS washing to remove OCT or deparaffinization and rehydration to remove paraffin, mouse samples were stained with Masson Trichrome staining (Sigma), Congo red staining (Sigma), and after either heat-induced or formic acid[109] antigen retrieval (water bath for 45 min at 90C in citric buffer pH 6.0 with 1% of tween-20), indirectly immunolabeled with commercially available primary antibodies (listed in key resources table) and corresponding fluorophore-conjugated secondary reagents (table) or directly stained for the Thioflavin S (Acros Organics) in green. Nuclei were counterstained with 4′,6-diamidino-2-phenylindole dihydrochloride (DAPI; Sigma-Aldrich). Rehydrated slides were also stained for Serum Amyloid A 1-3 after formic acid (70% formic acid in d.d. water) antigen retrieval (20 minutes at room temperature). Multiple sections from the hearts of at least seven mice for each treatment were examined, and representative treatments and time points are described in the results and the Figure's legend. Images were acquired either with a Nikon Eclipse Ti fluorescence microscope using 4X, 10X, 20X, and 40X objectives or EVOS 7000 (Thermo Fisher Scientific). Masson Trichrome staining images were acquired with a Nikon stereo-microscope at 1X (scar quantification) and a Nikon Eclipse NiE bright field and fluorescence microscope using 4X, 10X, and 20X in bright field. Congo red images were acquired using a Nikon E800 microscope and a digital color camera (Jenoptik Graphax® Kapella) linked to an image

analysis system (Bioquant, Life Science 2022 software version, Nashville, TN). Before the use of this microscope for polarized light visualization, a polarized filter was inserted into the appropriate upper slot of the microscope (above the revolving nose piece and below the observation tube), and a lower polarized filter that rotates 360° was attached below the stage (both by Nikon). In addition, the condenser was rotated to the correct differential interference contrast setting for the objective used (DIC-M for 20x and DIC-H for 40X objective, respectively). The Bioquant software's gain was very dark, and the gain of the red and green colors was set high. The rotation of the lower polarizing filter was slowly moved to approximately 90° until the collagen fibrils showed birefringence colors. Optical sections were projected into a single plane for each color channel and merged using Adobe Photoshop (Adobe) software. Quantitative image analysis was performed with NIH ImageJ by scoring blindly multiple imaging fields.

Single-cell sequencing—Single-cell RNA sequencing of MI hearts was performed as part of a previous study.[53] Using the 10x Chromium platform with v 2 Chemistry and analyzed using Cell Ranger v3 (as in https://www.ahajournals.org/doi/full/10.1161/CIRCULATIONAHA.120.044581?rfr_dat=cr_pub++0pubmed&url_ver=Z39.88-2003&rfr_id=ori%3Arid%3Acrossref.org).[53] Count Matrixes were processed in R version 4.3.1 (https://www.r-project.org/), using Seurat software package version 5.0, by filtering out objects with less than 200 and more than 5000 genes (nFeature_RNA) and a percent. mt over 25. Cell cycle regression, normalization, and scaling were performed on individual objects before merging them following the procedure described in the vignette: https://satijalab.org/seurat/v3.0/merge_vignette.html. The following parameters were used for the clustering: reduction = "pca", dims = 1:33, resolution = 0.5.

We want to clarify that the expression of PDPN did not drive nor influence the scRNA-seq clustering. Indeed, there is no clustering based on PDPN expression. We clustered the data using Seurat v3 and defined the clusters unbiasedly using the "FindNeighbours", and "FindClusters" functions on previously normalized and scaled data. Subsequently, we visualized PDPN expression through various plots: a FeaturePlot (Figure S1B), a Violin plot (Figure S1C), and a DotPlot (Figure S1D). The results indicated that PDPN expression is notably high in lymphatic endothelial cells, as expected, and is also upregulated in activated stromal cells at day 1 post- MI and in activated epicardium from days 3 to 28.

Small extracellular vesicles isolation and characterization—Small extracellular vesicles (sEVs-/exosomes) were isolated as described in our previous publications.[26,28,61,110] Briefly, 0.2μm filtered conditioned media was concentrated in Amicon ultra centrifugal filter conical tubes from Millipore with a cut-off of 100K, with multiple centrifugations at the maximum centrifugal speed. sEVs were then isolated with density-gradient ultracentrifugation, and sEVs size was analyzed with a nanoparticle tracking analyzer (Nanosight NS300), transmission electron microscopy and expression of exosomal marker proteins verified via Exo-Check™ Antibody Array (System Biosciences, Palo Alto, CA). To show the uptake of sEVs by BMDM, we labeled isolated sEVs with

PKH26 (in red), and we treated BMDM with labeled sEvs for 15, 30 minutes and 1 hour and image the cells after treatment.

Preparation of cell and tissue lysates and immunoblotting analysis—sEVs, cellular, and cardiac samples were homogenized using cell signaling technologies 1X lysis buffer (Cell Signaling technologies) enriched with phosphatases and protease inhibitors (Thermo Scientific). Specifically, cardiac samples were obtained by specific micro-dissection of infarcted and border zone areas from the rest of the heart (remote area). Lysates were then centrifuged for 10 min at 4°C at 13,000 rpm to discard the insoluble debris. Next, total protein amounts were quantified via a dye-binding Pierce BCA protein assay kit (Thermo Scientific) and detected using a spectrophotometer reader (SpectraMax i3x Multi-mode Microplate Reader, Molecular Devices) at a wavelength of 512 nm. Equal yields of protein (20-40 μg) were separated through SDS-PAGE and identified by western blot analysis. Total lysates were used to evaluate the exosomal, cellular, and cardiac protein levels. Protein bands were detected by using Odyssey® CLx Imaging System according to the manufacturer's instructions and quantified with Image Studio™ Lite Software.

Mass spectrometry analysis—Mass spectrometry analysis was performed by the CHOP-Children Hospital of Philadelphia core facility. Proteins were extracted from sEVs samples, denatured, reduced, alkylated, and digested into peptides. They were analyzed in a single shot on QE-HF in DIA mode in the LC-MS/MS analysis system. A spectral library was generated by MaxQuant (DDA), and proteins were quantified using Spectronaut software (DIA, Biognosys). Perseus was used for statistical analysis. Perseus transformed the data using log2, normalized the data by subtracting the median, and using a t-test to identify up/downregulated peptides/proteins between different samples. Biological function and process analysis was performed using gene ontology and KEGG software.

ELISA analysis—RayBiotech performed mouse cytokine and chemokine 92-plex discovery assay on cell culture supernatant of WT and TLR2 KO BMDM treated with different conditions. Cytokines profile was measured using a 92-plex luminex-based platform. SAA3 levels on CSC^{PDPN+} and mCECs were performed by Eve Technologies (Eve Technologies, Calgary, Canada)[20] on cell lysates using a Millipore ELISA kit. The SAA3 profile was measured using a 32-plex luminex-based platform. Based on the specific kit used by Eve Technologies, we performed ELISA quantification in-house using the same kit (Millipore) to quantify secreted SAA3 levels on BMDM-conditioned media after treatment with different conditions. SAA3 levels were detected using a spectrophotometer reader (SpectraMax i3x Multi-mode Microplate Reader, Molecular Devices) at a wavelength of 400 nm. The analysis was performed on three different biological samples for each condition.

Recombinant and synthesized proteins—Recombinant SAA3 was purchased from Biomatik and reconstituted in sterile water. DRI-R5S (sequence from N terminus to C terminus is SFFSR) was synthesized by Biomatik with serine at the N terminus and arginine at the C terminus with acetate salt endings to enhance the distribution in the tissues. DRI-

R5S was reconstituted in sterile and injectable saline water. SB 203580 compound was purchased at Cayman Chemical Company and reconstituted with DMSO.

Quantitative real-time PCR—Expression levels of different genes were measured using quantitative real-time (RT) PCR technology. Total cellular RNA was isolated from mouse cultured cells and mouse myocardial tissue (scar area and remote area separately) at 3, 7, and 30 days after MI, using miRNeasy Mini Kit (Qiagen) following the manufacturer's instructions.[20] The cDNA was obtained from total RNA using the high-capacity cDNA revere transcription kit (Applied Biosystems). RT–PCR was performed on an Applied Biosystems 770 apparatus. Full list of primers is listed in Table S3.

Computational analysis—Using long molecular dynamics simulations, it was proposed in ref.[60] that the peptide DRI-R5S (sequence: D-SFFSR), built from D-amino acids, inhibits the formation of SAA aggregates and de-stabilizes existing ones. For this peptide, we determined binding sites and the docking for human SAA1 cross-beta fibril structures and mouse SAA3, Fibronectin, and Collagen Iα using the HADDOCK[111] software. The PRODIGY[112] software approximated binding energies. We find that the DRI-RSFFS segment interacts with the following mouse SAA3 Monomer Residues: E27, A28, G31, S32, M35, W36, Y39, M42, K43, D51, H55, A62, G68, G69, A72, A73, I76, R80, V83, Q84, T87, H89. The DRI-RSFFS segment disrupts the monomer's interactions between helix 1 and 3 in its native conformation. A trimmed structure was used to model the effect of a cleaved peptide, similar to human SAA1 (1-76) fragments known to form fibril structures. The structure of the mouse SAA3 monomer was generated from the full mouse SAA3 monomer structure (PDB-ID: 6PXZ) by removing residues 90-122. The guanidinium group of the arginine residue of the DRI peptide nestles into a pocket in the surface of the monomer and contributes most to the interactions between the peptide and monomer (interacting with E27, A28, G31, S32, G68, G69, A72, A73). It should be noted that the DRI peptide interacts with E27 through its backbone atoms rather than its sidechain carboxylate group. The DRI-RSFFS segment interacts with the following Fibronectin Residues (PDB-ID: 1FBR): F5, D6, H7, L21, P22, Y23, M27, V29, G39, I41, T42, C43, T44, S45, R48, C49, N50, R83, G84, E85, W86. These interactions can be organized into three main clusters depending on the DRI residue: Cluster 1 (DRI-residue 1), Cluster 2 (DRI-residues 2-4), and Cluster 3 (DRI-residue 5). Cluster 1 (DRI-residue 1): F5, D6, H7, G39, I4, Cluster 2 (DRI-residues 2-4): L21, P22, Y23, M27, V29, I41, T42, C43, T44, S45, Cluster 3 (DRI-residue 5): T44, S45, R48, C49, N50, R83, G84, E85, W86. The Fibronectin residues of Cluster 3 form a pocket with which the C-terminal arginine residue of the DRI segment interacts. These interactions contribute to most of the contacts observed. Similarly, cluster 1 also forms a pocket on the protein's surface, interacting with the N-terminus of the DRI-peptide. Cluster 2 contributes to a grove that connects Zone 1 and Zone 3. The final DRI-RSFFS structure was derived from the N-terminal residues RSFFS of human SAA1(hSAA1), which inhibit SAA fibril formation,[108] by reversing the sequence and replacing the common L-amino acids with their D-amino acid analogs. The resulting DRI-peptides are structurally and functionally close to their L-parents, in our case, small hydrophilic and non-toxic molecules that are easily delivered to the organs. However, unlike its L-parents, DRI-R5S is resistant to proteolytic digestion and has a much longer lifetime.

Structural models of mouse SAA3 fibrils or oligomers have not been resolved. However, since the mouse SAA3 protein shares 69% amino acid identity with hSAA1 and that hSAA1 fibril structure has been resolved, we could assume in our mouse experiments that DRI-R5S would bind in a similar way to mouse SAA3 than to hSAA1, and that there are preserved aggregation sites (Figure 6A). Binding sites were determined with HADDOCK[111] software and the binding energies approximated by PRODIGY.[112] As shown, DRI-R5S docks either with mouse SAA3 (Figure 6A) or human SAA1 (Figure S5C) monomer's sites and simulations performed with fibrils configuration[113] (Figure S5D) identified that the free energies of binding from the original docking ranged from −23 (SAA1) to −36.4 (SAA3) kJ/mol with the DRI-R5S which is considered an excellent affinity for a small molecule.

QUANTIFICATION AND STATISTICAL ANALYSIS

All *in vitro* and *in vivo* experiments during the study period were performed blindly. Data are expressed as means ± SEM. A two-tailed Student's t-test determined the statistical significance between the two groups. When comparing multiple groups, data were analyzed using a one-way or two-way analysis of variance (ANOVA) test, followed by Tukey's post hoc test. Differences between groups were considered statistically significant when $p \leq 0.05$. All data were analyzed and graphically represented using GraphPad Prism software version 9 (GraphPad, La Jolla, CA). The type of statistical analysis and the number of biological replicates (number of animals or experimental replicates) used are denoted in the graphs of the figures and detailed in the figure legend.

Supplementary Material

Refer to Web version on PubMed Central for supplementary material.

ACKNOWLEDGMENTS

This research was funded in part by National Institutes of Health grants HL143892, HL134608, HL169405, and HL147841 (to R.K.) and American Heart Association Career Development Award (CDA) 23CDA1053810 (to M.C.). C.T. was supported by NIH AI 171568 and AI153325. U.H.E.H. was supported by GM120634. We want to thank Lynn Spruce, Technical Director, and Hossein Fazelinia, Principal Bioinformatics Scientist, of the Children Hospital of Philadelphia Research Institute Proteomics Core facility for help with the mass spectrometry data generation and analysis.

REFERENCES

1. Pour-Ghaz I, Bath A, Kayali S, Alkhatib D, Yedlapati N, Rhea I, Khouzam RN, Jefferies JL, and Nayyar M (2022). A Review of Cardiac Amyloidosis: Presentation, Diagnosis, and Treatment. Curr. Probl. Cardiol 47, 101366. 10.1016/j.cpcardiol.2022.101366. [PubMed: 35995246]
2. Wang W, and Hansmann UHE (2020). Stability of Human Serum Amyloid A Fibrils. J. Phys. Chem. B 124, 10708–10717. 10.1021/acs.jpcb.0c08280. [PubMed: 33197318]
3. Wang WS, Li WJ, Wang YW, Wang LY, Mi YB, Lu JW, Lu Y, Zhang CY, and Sun K (2019). Involvement of serum amyloid A1 in the rupture of fetal membranes through induction of collagen I degradation. Clin. Sci 133, 515–530. 10.1042/CS20180950.
4. Flodrova P, Flodr P, Pika T, Vymetal J, Holub D, Dzubak P, Hajduch M, and Scudla V (2018). Cardiac amyloidosis: from clinical suspicion to morphological diagnosis. Pathology 50, 261–268. 10.1016/j.pathol.2017.10.012. [PubMed: 29448998]
5. Pagourelias ED, Mirea O, Duchenne J, Van Cleemput J, Delforge M, Bogaert J, Kuznetsova T, and Voigt JU (2017). Echo Parameters for Differential Diagnosis in Cardiac Amyloidosis: A Head-

to-Head Comparison of Deformation and Nondeformation Parameters. Circ. Cardiovasc. Imaging 10, e005588. 10.1161/CIRCIMAGING.116.005588. [PubMed: 28298286]

6. Casl MT, Surina B, Glojnaric-Spasic I, Pape E, Jagarinec N, and Kranjcevic S (1995). Serum amyloid A protein in patients with acute myocardial infarction. Ann. Clin. Biochem 32, 196–200. 10.1177/000456329503200212. [PubMed: 7540381]
7. Clifton PM, Mackinnon AM, and Barter PJ (1985). Effects of serum amyloid A protein (SAA) on composition, size, and density of high density lipoproteins in subjects with myocardial infarction. J. Lipid Res 26, 1389–1398. [PubMed: 4086942]
8. Bausserman LL, Sadaniantz A, Saritelli AL, Martin VL, Nugent AM, Sady SP, and Herbert PN (1989). Time course of serum amyloid A response in myocardial infarction. Clin. Chim. Acta 184, 297–305. 10.1016/0009-8981(89)90063-6. [PubMed: 2515010]
9. Ji H, Chen S, Hu Q, He Y, Zhou L, Xie J, Pan H, Tong X, and Wu C (2024). Investigating the Correlation between Serum Amyloid A and Infarct-Related Artery Patency Prior to Percutaneous Coronary Intervention in ST-Segment Elevation Myocardial Infarction Patients. Angiology 75, 585–594. 10.1177/00033197231183031. [PubMed: 37402552]
10. Kosuge M, Ebina T, Ishikawa T, Hibi K, Tsukahara K, Okuda J, Iwahashi N, Ozaki H, Yano H, Kusama I, et al. (2007). Serum amyloid A is a better predictor of clinical outcomes than C-reactive protein in non-ST-segment elevation acute coronary syndromes. Circ. J 71, 186–190. 10.1253/circj.71.186. [PubMed: 17251664]
11. Johnson BD, Kip KE, Marroquin OC, Ridker PM, Kelsey SF, Shaw LJ, Pepine CJ, Sharaf B, Bairey Merz CN, Sopko G, et al. (2004). Serum amyloid A as a predictor of coronary artery disease and cardiovascular outcome in women: the National Heart, Lung, and Blood Institute-Sponsored Women's Ischemia Syndrome Evaluation (WISE). Circulation 109, 726–732. 10.1161/01.CIR.0000115516.54550.B1. [PubMed: 14970107]
12. Katayama T, Nakashima H, Honda Y, Suzuki S, Yamamoto T, Iwasaki Y, and Yano K (2007). The relationship between acute phase serum amyloid A (SAA) protein concentrations and left ventricular systolic function in acute myocardial infarction patients treated with primary coronary angioplasty. Int. Heart J 48, 45–55. 10.1536/ihj.48.45. [PubMed: 17379978]
13. Katayama T, Nakashima H, Takagi C, Honda Y, Suzuki S, Iwasaki Y, Yamamoto T, Yoshioka M, and Yano K (2006). Serum amyloid a protein as a predictor of cardiac rupture in acute myocardial infarction patients following primary coronary angioplasty. Circ. J 70, 530–535. 10.1253/circj.70.530. [PubMed: 16636485]
14. Katayama T, Nakashima H, Takagi C, Honda Y, Suzuki S, Iwasaki Y, and Yano K (2005). Prognostic value of serum amyloid A protein in patients with acute myocardial infarction. Circ. J 69, 1186–1191. 10.1253/circj.69.1186. [PubMed: 16195614]
15. Morrow DA, Rifai N, Antman EM, Weiner DL, McCabe CH, Cannon CP, and Braunwald E (2000). Serum amyloid A predicts early mortality in acute coronary syndromes: A TIMI 11A substudy. J. Am. Coll. Cardiol 35, 358–362. 10.1016/s0735-1097(99)00574-4. [PubMed: 10676681]
16. Garcia-Garcia E, Gonzalez-Romero GM, Martin-Perez EM, Zapata Cornejo ED, Escobar-Aguilar G, and Cardenas Bonnet MF (2021). Real-World Data and Machine Learning to Predict Cardiac Amyloidosis. Int. J. Environ. Res. Public Health 18, 908. 10.3390/ijerph18030908. [PubMed: 33494357]
17. Pislaru C, Ionescu F, Alashry M, Petrescu I, Pellikka PA, Grogan M, Dispenzieri A, and Pislaru SV (2019). Myocardial Stiffness by Intrinsic Cardiac Elastography in Patients with Amyloidosis: Comparison with Chamber Stiffness and Global Longitudinal Strain. J. Am. Soc. Echocardiogr 32, 958–968.e4. 10.1016/j.echo.2019.04.418. [PubMed: 31230779]
18. Arani A, Arunachalam SP, Chang ICY, Baffour F, Rossman PJ, Glaser KJ, Trzasko JD, McGee KP, Manduca A, Grogan M, et al. (2017). Cardiac MR elastography for quantitative assessment of elevated myocardial stiffness in cardiac amyloidosis. J. Magn. Reson. Imaging 46, 1361–1367. 10.1002/jmri.25678. [PubMed: 28236336]
19. Cimini M, Cannatá A, Pasquinelli G, Rota M, and Goichberg P (2017). Phenotypically heterogeneous podoplanin-expressing cell populations are associated with the lymphatic vessel growth and fibrogenic responses in the acutely and chronically infarcted myocardium. PLoS One 12, e0173927. 10.1371/journal.pone.0173927. [PubMed: 28333941]

20. Cimini M, Garikipati VNS, de Lucia C, Cheng Z, Wang C, Truongcao MM, Lucchese AM, Roy R, Benedict C, Goukassian DA, et al. (2019). Podoplanin neutralization improves cardiac remodeling and function after acute myocardial infarction. JCI Insight 5, e126967. 10.1172/jci.insight.126967. [PubMed: 31287805]
21. Cimini M, and Kishore R (2021). Role of Podoplanin-Positive Cells in Cardiac Fibrosis and Angiogenesis After Ischemia. Front. Physiol 12, 667278. 10.3389/fphys.2021.667278. [PubMed: 33912076]
22. Pollitt AY, Poulter NS, Gitz E, Navarro-Nuñez L, Wang YJ, Hughes CE, Thomas SG, Nieswandt B, Douglas MR, Owen DM, et al. (2014). Syk and Src family kinases regulate C-type lectin receptor 2 (CLEC-2)-mediated clustering of podoplanin and platelet adhesion to lymphatic endothelial cells. J. Biol. Chem 289, 35695–35710. 10.1074/jbc.M114.584284. [PubMed: 25368330]
23. Valente S, Rossi R, Resta L, and Pasquinelli G (2015). Exploring the human mesenchymal stem cell tubule communication network through electron microscopy. Ultrastruct. Pathol 39, 88–94. 10.3109/01913123.2014.960545. [PubMed: 25268461]
24. Garikipati VNS, and Kishore R (2018). Induced Pluripotent Stem Cells Derived Extracellular Vesicles: A Potential Therapy for Cardiac Repair. Circ. Res 122, 197–198. 10.1161/CIRCRESAHA.117.312394. [PubMed: 29348245]
25. Garikipati VNS, Shoja-Taheri F, Davis ME, and Kishore R (2018). Extracellular Vesicles and the Application of System Biology and Computational Modeling in Cardiac Repair. Circ. Res 123, 188–204. 10.1161/CIRCRESAHA.117.311215. [PubMed: 29976687]
26. Cheng Z, Naga Srikanth Garikipati V, Truongcao MM, Cimini M, Huang G, Wang C, Benedict C, Gonzalez C, Mallaredy V, Goukassian DA, et al. (2021). Serum-Derived Small Extracellular Vesicles From Diabetic Mice Impair Angiogenic Property of Microvascular Endothelial Cells: Role of EZH2. J. Am. Heart Assoc 10, e019755. 10.1161/JAHA.120.019755. [PubMed: 33988033]
27. Zazzeroni L, Faggioli G, and Pasquinelli G (2018). Mechanisms of Arterial Calcification: The Role of Matrix Vesicles. Eur. J. Vasc. Endovasc. Surg 55, 425–432. 10.1016/j.ejvs.2017.12.009. [PubMed: 29371036]
28. Yue Y, Wang C, Benedict C, Huang G, Truongcao M, Roy R, Cimini M, Garikipati VNS, Cheng Z, Koch WJ, and Kishore R (2020). Interleukin-10 Deficiency Alters Endothelial Progenitor Cell-Derived Exosome Reparative Effect on Myocardial Repair via Integrin-Linked Kinase Enrichment. Circ. Res 126, 315–329. 10.1161/CIRCRESAHA.119.315829. [PubMed: 31815595]
29. Tannock LR, De Beer MC, Ji A, Shridas P, Noffsinger VP, den Hartigh L, Chait A, De Beer FC, and Webb NR (2018). Serum amyloid A3 is a high density lipoprotein-associated acute-phase protein. J. Lipid Res 59, 339–347. 10.1194/jlr.M080887. [PubMed: 29247043]
30. Yasar F, Sheridan MS, and Hansmann UHE (2022). Interconversion between Serum Amyloid A Native and Fibril Conformations. ACS Omega 7, 12186–12192. 10.1021/acsomega.2c00566. [PubMed: 35449919]
31. Ye RD, and Sun L (2015). Emerging functions of serum amyloid A in inflammation. J. Leukoc. Biol 98, 923–929. 10.1189/jlb.3VMR0315-080R. [PubMed: 26130702]
32. Sack GH Jr. (2018). Serum amyloid A - a review. Mol. Med 24, 46. 10.1186/s10020-018-0047-0. [PubMed: 30165816]
33. Uhlar CM, and Whitehead AS (1999). Serum amyloid A, the major vertebrate acute-phase reactant. Eur. J. Biochem 265, 501–523. 10.1046/j.1432-1327.1999.00657.x. [PubMed: 10504381]
34. De Buck M, Gouwy M, Wang JM, Van Snick J, Opdenakker G, Struyf S, and Van Damme J (2016). Structure and Expression of Different Serum Amyloid A (SAA) Variants and their Concentration-Dependent Functions During Host Insults. Curr. Med. Chem 23, 1725–1755. 10.2174/0929867323666160418114600. [PubMed: 27087246]
35. Thorn CF, and Whitehead AS (2002). Differential transcription of the mouse acute phase serum amyloid A genes in response to pro-inflammatory cytokines. Amyloid 9, 229–236. 10.3109/13506120209114098. [PubMed: 12557750]

36. Tomita T, Ieguchi K, Sawamura T, and Maru Y (2015). Human serum amyloid A3 (SAA3) protein, expressed as a fusion protein with SAA2, binds the oxidized low density lipoprotein receptor. PLoS One 10, e0118835. 10.1371/journal.pone.0118835. [PubMed: 25738827]
37. Chiba T, Han CY, Vaisar T, Shimokado K, Kargi A, Chen MH, Wang S, McDonald TO, O'Brien KD, Heinecke JW, and Chait A (2009). Serum amyloid A3 does not contribute to circulating SAA levels. J. Lipid Res 50, 1353–1362. 10.1194/jlr.M900089-JLR200. [PubMed: 19286646]
38. Chait A, den Hartigh LJ, Wang S, Goodspeed L, Babenko I, Altemeier WA, and Vaisar T (2020). Presence of serum amyloid A3 in mouse plasma is dependent on the nature and extent of the inflammatory stimulus. Sci. Rep 10, 10397. 10.1038/s41598-020-66898-7. [PubMed: 32587356]
39. Deguchi A, Tomita T, Omori T, Komatsu A, Ohto U, Takahashi S, Tanimura N, Akashi-Takamura S, Miyake K, and Maru Y (2013). Serum amyloid A3 binds MD-2 to activate p38 and NF-κB pathways in a MyD88-dependent manner. J. Immunol 191, 1856–1864. 10.4049/jimmunol.1201996. [PubMed: 23858030]
40. Cheng N, He R, Tian J, Ye PP, and Ye RD (2008). Cutting edge: TLR2 is a functional receptor for acute-phase serum amyloid A. J. Immunol 181, 22–26. 10.4049/jimmunol.181.1.22. [PubMed: 18566366]
41. Jayaraman S, Gantz DL, Haupt C, and Gursky O (2017). Serum amyloid A forms stable oligomers that disrupt vesicles at lysosomal pH and contribute to the pathogenesis of reactive amyloidosis. Proc. Natl. Acad. Sci. USA 114, E6507–E6515. 10.1073/pnas.1707120114. [PubMed: 28743750]
42. Berhanu WM, and Hansmann UHE (2014). Stability of amyloid oligomers. Adv. Protein Chem. Struct. Biol 96, 113–141. 10.1016/bs.apcsb.2014.06.006. [PubMed: 25443956]
43. Wang W, Khatua P, and Hansmann UHE (2020). Cleavage, Downregulation, and Aggregation of Serum Amyloid A. J. Phys. Chem. B 124, 1009–1019. 10.1021/acs.jpcb.9b10843. [PubMed: 31955564]
44. Papa R, and Lachmann HJ (2018). Secondary, AA, Amyloidosis. Rheum. Dis. Clin. North Am 44, 585–603. 10.1016/j.rdc.2018.06.004. [PubMed: 30274625]
45. Kryndushkin D, Wear MP, and Shewmaker F (2013). Amyloid cannot resist identification. Prion 7, 464–468. 10.4161/pri.27503. [PubMed: 24366087]
46. Jana AK, Greenwood AB, and Hansmann UHE (2021). Small Peptides for Inhibiting Serum Amyloid A Aggregation. ACS Med. Chem. Lett 12, 1613–1621. 10.1021/acsmedchemlett.1c00456. [PubMed: 34676044]
47. Doti N, Mardirossian M, Sandomenico A, Ruvo M, and Caporale A (2021). Recent Applications of Retro-Inverso Peptides. Int. J. Mol. Sci 22, 8677. 10.3390/ijms22168677. [PubMed: 34445382]
48. Lander AJ, Jin Y, and Luk LYP (2023). D-Peptide and D-Protein Technology: Recent Advances, Challenges, and Opportunities. Chembiochem 24, e202200537. 10.1002/cbic.202200537. [PubMed: 36278392]
49. Garton M, Nim S, Stone TA, Wang KE, Deber CM, and Kim PM (2018). Method to generate highly stable D-amino acid analogs of bioactive helical peptides using a mirror image of the entire PDB. Proc. Natl. Acad. Sci. USA 115, 1505–1510. 10.1073/pnas.1711837115. [PubMed: 29378946]
50. Liu M, Li X, Xie Z, Xie C, Zhan C, Hu X, Shen Q, Wei X, Su B, Wang J, and Lu W (2016). D-Peptides as Recognition Molecules and Therapeutic Agents. Chem. Rec 16, 1772–1786. 10.1002/tcr.201600005. [PubMed: 27255896]
51. Zimmermann O, and Hansmann UHE (2008). Understanding protein folding: small proteins in silico. Biochim. Biophys. Acta 1784, 252–258. 10.1016/j.bbapap.2007.10.010. [PubMed: 18036571]
52. Cabri W, Cantelmi P, Corbisiero D, Fantoni T, Ferrazzano L, Martelli G, Mattellone A, and Tolomelli A (2021). Therapeutic Peptides Targeting PPI in Clinical Development: Overview, Mechanism of Action and Perspectives. Front. Mol. Biosci 8, 697586. 10.3389/fmolb.2021.697586. [PubMed: 34195230]
53. Forte E, Skelly DA, Chen M, Daigle S, Morelli KA, Hon O, Philip VM, Costa MW, Rosenthal NA, and Furtado MB (2020). Dynamic Interstitial Cell Response during Myocardial Infarction Predicts Resilience to Rupture in Genetically Diverse Mice. Cell Rep. 30, 3149–3163.e6. 10.1016/j.celrep.2020.02.008. [PubMed: 32130914]

54. Sreejit G, Abdel-Latif A, Athmanathan B, Annabathula R, Dhyani A, Noothi SK, Quaife-Ryan GA, Al-Sharea A, Pernes G, Dragoljevic D, et al. (2020). Neutrophil-Derived S100A8/A9 Amplify Granulopoiesis After Myocardial Infarction. Circulation 141, 1080–1094. 10.1161/CIRCULATIONAHA.119.043833. [PubMed: 31941367]
55. Sreejit G, Nooti SK, Jaggers RM, Athmanathan B, Ho Park K, Al-Sharea A, Johnson J, Dahdah A, Lee MKS, Ma J, et al. (2022). Retention of the NLRP3 Inflammasome-Primed Neutrophils in the Bone Marrow Is Essential for Myocardial Infarction-Induced Granulopoiesis. Circulation 145, 31–44. 10.1161/CIRCULATIONAHA.121.056019. [PubMed: 34788059]
56. Kologrivova I, Shtatolkina M, Suslova T, and Ryabov V (2021). Cells of the Immune System in Cardiac Remodeling: Main Players in Resolution of Inflammation and Repair After Myocardial Infarction. Front. Immunol 12, 664457. 10.3389/fimmu.2021.664457. [PubMed: 33868315]
57. Lu S, and Qiao X (2021). Single-cell profiles of human bone marrow-derived mesenchymal stromal cells after IFN-gamma and TNF-alpha licensing. Gene 771, 145347. 10.1016/j.gene.2020.145347. [PubMed: 33333228]
58. Apostolaki M, Armaka M, Victoratos P, and Kollias G (2010). Cellular mechanisms of TNF function in models of inflammation and autoimmunity. Curr. Dir. Autoimmun 11, 1–26. 10.1159/000289195. [PubMed: 20173385]
59. Prockop DJ, and Oh JY (2012). Mesenchymal stem/stromal cells (MSCs): role as guardians of inflammation. Mol. Ther 20, 14–20. 10.1038/mt.2011.211. [PubMed: 22008910]
60. Volpe M, Mancia G, and Trimarco B (2005). Angiotensin II receptor blockers and myocardial infarction: deeds and misdeeds. J. Hypertens 23, 2113–2118. 10.1097/01.hjh.0000194114.12228.16. [PubMed: 16269950]
61. Khan M, Nickoloff E, Abramova T, Johnson J, Verma SK, Krishnamurthy P, Mackie AR, Vaughan E, Garikipati VNS, Benedict C, et al. (2015). Embryonic stem cell-derived exosomes promote endogenous repair mechanisms and enhance cardiac function following myocardial infarction. Circ. Res 117, 52–64. 10.1161/CIRCRESAHA.117.305990. [PubMed: 25904597]
62. Srinivasan S, Vannberg FO, and Dixon JB (2016). Lymphatic transport of exosomes as a rapid route of information dissemination to the lymph node. Sci. Rep 6, 24436. 10.1038/srep24436. [PubMed: 27087234]
63. Lee JY, Hall JA, Kroehling L, Wu L, Najar T, Nguyen HH, Lin WY, Yeung ST, Silva HM, Li D, et al. (2020). Serum Amyloid A Proteins Induce Pathogenic Th17 Cells and Promote Inflammatory Disease. Cell 183, 2036–2039. 10.1016/j.cell.2020.12.008. [PubMed: 33357400]
64. Yoo J, Lee SK, Lim M, Sheen D, Choi EH, and Kim SA (2017). Exosomal amyloid A and lymphatic vessel endothelial hyaluronic acid receptor-1 proteins are associated with disease activity in rheumatoid arthritis. Arthritis Res. Ther 19, 119. 10.1186/s13075-017-1334-9. [PubMed: 28569211]
65. Parry TL, Melehani JH, Ranek MJ, and Willis MS (2015). Functional Amyloid Signaling via the Inflammasome, Necrosome, and Signalosome: New Therapeutic Targets in Heart Failure. Front. Cardiovasc. Med 2, 25. 10.3389/fcvm.2015.00025. [PubMed: 26664897]
66. Wooten RM, Ma Y, Yoder RA, Brown JP, Weis JH, Zachary JF, Kirschning CJ, and Weis JJ (2002). Toll-like receptor 2 plays a pivotal role in host defense and inflammatory response to Borrelia burgdorferi. Vector Borne Zoonotic Dis. 2, 275–278. 10.1089/153036602321653860. [PubMed: 12804169]
67. Wooten RM, Ma Y, Yoder RA, Brown JP, Weis JH, Zachary JF, Kirschning CJ, and Weis JJ (2002). Toll-like receptor 2 is required for innate, but not acquired, host defense to Borrelia burgdorferi. J. Immunol 168, 348–355. 10.4049/jimmunol.168.1.348. [PubMed: 11751980]
68. Mallaredy V, Roy R, Cheng Z, Thej C, Benedict C, Truongcao M, Joladarashi D, Magadum A, Ibetti J, Cimini M, et al. (2024). Tipifarnib Reduces Extracellular Vesicles and Protects From Heart Failure. Circ. Res 135, 280–297. 10.1161/CIRCRESAHA.123.324110. [PubMed: 38847080]
69. Ebert R, Benisch P, Krug M, Zeck S, Meißner-Weigl J, Steinert A, Rauner M, Hofbauer L, and Jakob F (2015). Acute phase serum amyloid A induces proinflammatory cytokines and mineralization via toll-like receptor 4 in mesenchymal stem cells. Stem Cell Res. 15, 231–239. 10.1016/j.scr.2015.06.008. [PubMed: 26135899]

70. Lu J, Yu Y, Zhu I, Cheng Y, and Sun PD (2014). Structural mechanism of serum amyloid A-mediated inflammatory amyloidosis. Proc. Natl. Acad. Sci. USA 111, 5189–5194. 10.1073/pnas.1322357111. [PubMed: 24706838]
71. Meek RL, Eriksen N, and Benditt EP (1992). Murine serum amyloid A3 is a high density apolipoprotein and is secreted by macrophages. Proc. Natl. Acad. Sci. USA 89, 7949–7952. 10.1073/pnas.89.17.7949. [PubMed: 1518819]
72. Chen MZ, Moily NS, Bridgford JL, Wood RJ, Radwan M, Smith TA, Song Z, Tang BZ, Tilley L, Xu X, et al. (2017). A thiol probe for measuring unfolded protein load and proteostasis in cells. Nat. Commun 8, 474. 10.1038/s41467-017-00203-5. [PubMed: 28883394]
73. Howie AJ, Brewer DB, Howell D, and Jones AP (2008). Physical basis of colors seen in Congo red-stained amyloid in polarized light. Lab. Invest 88, 232–242. 10.1038/labinvest.3700714. [PubMed: 18166974]
74. El-Meanawy A, Mueller C, and Iczkowski KA (2019). Improving sensitivity of amyloid detection by Congo red stain by using polarizing microscope and avoiding pitfalls. Diagn. Pathol 14, 57. 10.1186/s13000-019-0822-4. [PubMed: 31200733]
75. Gregoire S, Irwin J, and Kwon I (2012). Techniques for Monitoring Protein Misfolding and Aggregation in Vitro and in Living Cells. Korean J. Chem. Eng 29, 693–702. 10.1007/s11814-012-0060-x. [PubMed: 23565019]
76. Saxena A, Russo I, and Frangogiannis NG (2016). Inflammation as a therapeutic target in myocardial infarction: learning from past failures to meet future challenges. Transl. Res 167, 152–166. 10.1016/j.trsl.2015.07.002. [PubMed: 26241027]
77. Rösener NS, Gremer L, Reinartz E, Konig A, Brener O, Heise H, Hoyer W, Neudecker P, and Willbold D. (2018). A d-enantiomeric peptide interferes with heteroassociation of amyloid-β oligomers and prion protein. J. Biol. Chem 293, 15748–15764. 10.1074/jbc.RA118.003116. [PubMed: 30131337]
78. Aillaud I, Kaniyappan S, Chandupatla RR, Ramirez LM, Alkhashrom S, Eichler J, Horn AHC, Zweckstetter M, Mandelkow E, Sticht H, and Funke SA (2022). A novel D-amino acid peptide with therapeutic potential (ISAD1) inhibits aggregation of neurotoxic disease-relevant mutant Tau and prevents Tau toxicity in vitro. Alzheimers Res. Ther 14, 15. 10.1186/s13195-022-00959-z. [PubMed: 35063014]
79. Parthsarathy V, McClean PL, Holscher C, Taylor M, Tinker C, Jones G, Kolosov O, Salvati E, Gregori M, Masserini M, and Allsop D (2013). A novel retro-inverso peptide inhibitor reduces amyloid deposition, oxidation and inflammation and stimulates neurogenesis in the APPswe/PS1DeltaE9 mouse model of Alzheimer's disease. PLoS One 8, e54769. 10.1371/journal.pone.0054769. [PubMed: 23382963]
80. Diomede L, Zanier ER, Moro F, Vegliante G, Colombo L, Russo L, Cagnotto A, Natale C, Xodo FM, De Luigi A, et al. (2023). Aβ1-6_{A2V}(D) peptide, effective on Aβ aggregation, inhibits tau misfolding and protects the brain after traumatic brain injury. Mol. Psychiatry 28, 2433–2444. 10.1038/s41380-023-02101-3. [PubMed: 37198260]
81. Gandbhir O, and Sundaram P (2019). Pre-Clinical Safety and Efficacy Evaluation of Amytrap, a Novel Therapeutic to Treat Alzheimer's Disease. J. Alzheimers Dis. Rep 3, 77–94. 10.3233/ADR-190107. [PubMed: 31259305]
82. Schemmert S, Camargo LC, Honold D, Gering I, Kutzsche J, Willuweit A, and Willbold D (2021). In Vitro and In Vivo Efficacies of the Linear and the Cyclic Version of an All-d-Enantiomeric Peptide Developed for the Treatment of Alzheimer's Disease. Int. J. Mol. Sci 22, 6553. 10.3390/ijms22126553. [PubMed: 34207233]
83. Stark T, Lieblein T, Pohland M, Kalden E, Freund P, Zangl R, Grewal R, Heilemann M, Eckert GP, Morgner N, and Göbel MW (2017). Peptidomimetics That Inhibit and Partially Reverse the Aggregation of $Aβ_{1-42}$. Biochemistry 56, 4840–4849. 10.1021/acs.biochem.7b00223. [PubMed: 28841311]
84. Taylor M, Moore S, Mayes J, Parkin E, Beeg M, Canovi M, Gobbi M, Mann DMA, and Allsop D (2010). Development ofa proteolytically stable retro-inverso peptide inhibitor of beta-amyloid oligomerization as a potential novel treatment for Alzheimer's disease. Biochemistry 49, 3261–3272. 10.1021/bi100144m. [PubMed: 20230062]

85. Ather JL, and Poynter ME (2018). Serum amyloid A3 is required for normal weight and immunometabolic function in mice. PLoS One 13, e0192352. 10.1371/journal.pone.0192352. [PubMed: 29390039]

86. Forte E, Furtado MB, and Rosenthal N (2018). The interstitium in cardiac repair: role of the immune-stromal cell interplay. Nat. Rev. Cardiol 15, 601–616. 10.1038/s41569-018-0077-x. [PubMed: 30181596]

87. Tzahor E, and Dimmeler S (2022). A coalition to heal-the impact of the cardiac microenvironment. Science 377, eabm4443. 10.1126/science.abm4443. [PubMed: 36048959]

88. Chimenti I, Gaetani R, and Pagano F (2023). Editorial: The cardiac stroma in homeostasis and disease. Front. Cardiovasc. Med 10, 1248750. 10.3389/fcvm.2023.1248750. [PubMed: 37492159]

89. Chimenti I, Sattler S, Del Monte-Nieto G, and Forte E (2021). Editorial: Fibrosis and Inflammation in Tissue Pathophysiology. Front. Physiol 12, 830683. 10.3389/fphys.2021.830683. [PubMed: 35126187]

90. Quijada P, Trembley MA, and Small EM (2020). The Role of the Epicardium During Heart Development and Repair. Circ. Res 126, 377–394. 10.1161/CIRCRESAHA.119.315857. [PubMed: 31999538]

91. Ward LSC, Sheriff L, Marshall JL, Manning JE, Brill A, Nash GB, and McGettrick HM (2019). Podoplanin regulates the migration of mesenchymal stromal cells and their interaction with platelets. J. Cell Sci 132, jcs222067. 10.1242/jcs.222067. [PubMed: 30745334]

92. Yaghi OK, Hanna BS, Langston PK, Michelson DA, Jayewickreme T, Marin-Rodero M, Benoist C, and Mathis D (2023). A discrete 'early-responder' stromal-cell subtype orchestrates immunocyte recruitment to injured tissue. Nat. Immunol 24, 2053–2067. 10.1038/s41590-023-01669-w. [PubMed: 37932455]

93. Farbehi N, Patrick R, Dorison A, Xaymardan M, Janbandhu V, Wystub-Lis K, Ho JW, Nordon RE, and Harvey RP (2019). Single-cell expression profiling reveals dynamic flux of cardiac stromal, vascular and immune cells in health and injury. Elife 8, e43882. 10.7554/eLife.43882. [PubMed: 30912746]

94. Yang Y, García-Verdugo JM, Soriano-Navarro M, Srinivasan RS, Scallan JP, Singh MK, Epstein JA, and Oliver G. (2012). Lymphatic endothelial progenitors bud from the cardinal vein and intersomitic vessels in mammalian embryos. Blood 120, 2340–2348. 10.1182/blood-2012-05-428607. [PubMed: 22859612]

95. Douglas YL, Mahtab EAF, Jongbloed MRM, Uhrin P, Zaujec J, Binder BR, Schalij MJ, Poelmann RE, Deruiter MC, and Gittenberger-de Groot AC (2009). Pulmonary vein, dorsal atrial wall and atrial septum abnormalities in podoplanin knockout mice with disturbed posterior heart field contribution. Pediatr. Res 65, 27–32. 10.1203/PDR.0b013e31818bc11a. [PubMed: 18784615]

96. Gittenberger-de Groot AC, Mahtab EAF, Hahurij ND, Wisse LJ, Deruiter MC, Wijffels MCEF, and Poelmann RE (2007). Nkx2.5-negative myocardium of the posterior heart field and its correlation with podoplanin expression in cells from the developing cardiac pacemaking and conduction system. Anat. Rec 290, 115–122. 10.1002/ar.20406.

97. Mahtab EAF, Wijffels MCEF, Van Den Akker NMS, Hahurij ND, Lie-Venema H, Wisse LJ, Deruiter MC, Uhrin P, Zaujec J, Binder BR, et al. (2008). Cardiac malformations and myocardial abnormalities in podoplanin knockout mouse embryos: Correlation with abnormal epicardial development. Dev. Dyn 237, 847–857. 10.1002/dvdy.21463. [PubMed: 18265012]

98. Pan Y, and Xia L (2015). Emerging roles of podoplanin in vascular development and homeostasis. Front. Med 9, 421–430. 10.1007/s11684-015-0424-9. [PubMed: 26498027]

99. Tamura S, Mukaide M, Katsuragi Y, Fujii W, Odaira K, Suzuki N, Tsukiji N, Okamoto S, Suzuki A, Kanematsu T, et al. (2022). Periosteum-derived podoplanin-expressing stromal cells regulate nascent vascularization during epiphyseal marrow development. J. Biol. Chem 298, 101833. 10.1016/j.jbc.2022.101833. [PubMed: 35304101]

100. Lim SE, Joseph MD, de Winde CM, Acton SE, and Simoncelli S (2023). Quantitative single molecule analysis of podoplanin clustering in fibroblastic reticular cells uncovers CD44 function. Open Biol. 13, 220377. 10.1098/rsob.220377. [PubMed: 37161290]

101. Astarita JL, Cremasco V, Fu J, Darnell MC, Peck JR, Nieves-Bonilla JM, Song K, Kondo Y, Woodruff MC, Gogineni A, et al. (2015). The CLEC-2-podoplanin axis controls the contractility

of fibroblastic reticular cells and lymph node microarchitecture. Nat. Immunol 16, 75–84. 10.1038/ni.3035. [PubMed: 25347465]

102. Acton SE, Astarita JL, Malhotra D, Lukacs-Kornek V, Franz B, Hess PR, Jakus Z, Kuligowski M, Fletcher AL, Elpek KG, et al. (2012). Podoplanin-rich stromal networks induce dendritic cell motility via activation of the C-type lectin receptor CLEC-2. Immunity 37, 276–289. 10.1016/j.immuni.2012.05.022. [PubMed: 22884313]
103. Meng D, Luo M, and Liu B (2021). The Role of CLEC-2 and Its Ligands in Thromboinflammation. Front. Immunol 12, 688643. 10.3389/fimmu.2021.688643. [PubMed: 34177942]
104. Meng D, Ma X, Li H, Wu X, Cao Y, Miao Z, and Zhang X (2021). A Role of the Podoplanin-CLEC-2 Axis in Promoting Inflammatory Response After Ischemic Stroke in Mice. Neurotox. Res 39, 477–488. 10.1007/s12640-020-00295-w. [PubMed: 33165736]
105. Maier W, Altwegg LA, Corti R, Gay S, Hersberger M, Maly FE, Sütsch G, Roffi M, Neidhart M, Eberli FR, et al. (2005). Inflammatory markers at the site of ruptured plaque in acute myocardial infarction: locally increased interleukin-6 and serum amyloid A but decreased C-reactive protein. Circulation 111, 1355–1361. 10.1161/01.CIR.0000158479.58589.0A. [PubMed: 15753219]
106. Skibiszewska S, Żaczek S, Dybala-Defratyka A, Jędrzejewska K, and Jankowska E (2020). Influence of short peptides with aromatic amino acid residues on aggregation properties of serum amyloid A and its fragments. Arch. Biochem. Biophys 681, 108264. 10.1016/j.abb.2020.108264. [PubMed: 31945312]
107. Sosnowska M, Skibiszewska S, Kamińska E, Wieczerzak E, and Jankowska E (2016). Designing peptidic inhibitors of serum amyloid A aggregation process. Amino Acids 48, 1069–1078. 10.1007/s00726-015-2167-y. [PubMed: 26759015]
108. Sano T, Huang W, Hall JA, Yang Y, Chen A, Gavzy SJ, Lee JY, Ziel JW, Miraldi ER, Domingos AI, et al. (2016). An IL-23R/IL-22 Circuit Regulates Epithelial Serum Amyloid A to Promote Local Effector Th17 Responses. Cell 164, 324. 10.1016/j.cell.2015.12.047. [PubMed: 28915371]
109. Christensen DZ, Bayer TA, and Wirths O (2009). Formic acid is essential for immunohistochemical detection of aggregated intraneuronal Abeta peptides in mouse models of Alzheimer's disease. Brain Res. 1301, 116–125. 10.1016/j.brainres.2009.09.014. [PubMed: 19751708]
110. Garikipati VNS, Krishnamurthy P, Verma SK, Khan M, Abramova T, Mackie AR, Qin G, Benedict C, Nickoloff E, Johnson J, et al. (2015). Negative Regulation of miR-375 by Interleukin-10 Enhances Bone Marrow-Derived Progenitor Cell-Mediated Myocardial Repair and Function After Myocardial Infarction. Stem Cells 33, 3519–3529. 10.1002/stem.2121. [PubMed: 26235810]
111. van Zundert GCP, Rodrigues JPGLM, Trellet M, Schmitz C, Kastritis PL, Karaca E, Melquiond ASJ, van Dijk M, de Vries SJ, and Bonvin AMJJ (2016). The HADDOCK2.2 Web Server: User-Friendly Integrative Modeling of Biomolecular Complexes. J. Mol. Biol 428, 720–725. 10.1016/j.jmb.2015.09.014. [PubMed: 26410586]
112. Xue LC, Rodrigues JP, Kastritis PL, Bonvin AM, and Vangone A (2016). PRODIGY: a web server for predicting the binding affinity of protein-protein complexes. Bioinformatics 32, 3676–3678. 10.1093/bioinformatics/btw514. [PubMed: 27503228]
113. Trott O, and Olson AJ (2010). AutoDock Vina: improving the speed and accuracy of docking with a new scoring function, efficient optimization, and multithreading. J. Comput. Chem 31, 455–461. 10.1002/jcc.21334. [PubMed: 19499576]

Highlights

- Identification of serum amyloid A (SAA) 3 amyloidosis after myocardial infarction (MI)
- Exosomes derived from cardiac stromal cells positive for Podoplanin are enriched in SAA3
- Exosomal SAA3 triggers SAA3 overproduction in macrophages
- Retro-inverso D-peptide abrogates SAA3 amyloidosis, improving cardiac function after MI

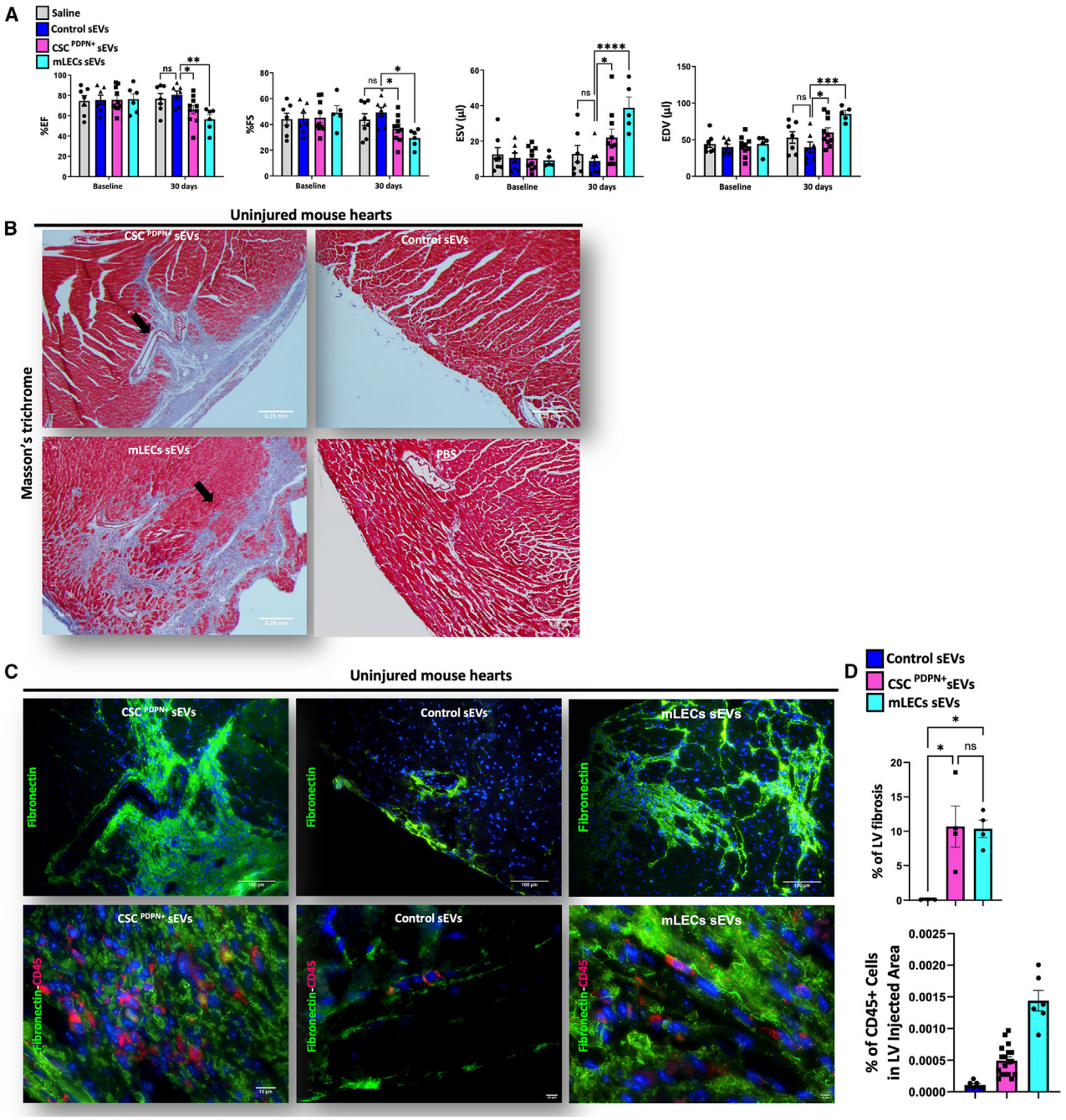

Figure 1. CSC^{PDPN+} sEVs impair cardiac function in healthy mouse hearts

(A) Echocardiography analysis showed a reduction of percent ejection fraction (%EF) and fractional shorting (FS) and an increase in end-systolic volume (ESV) and end-diastolic volume (EDV) in healthy mouse hearts injected with sEVs derived from pretreated CSC^{PDPN+} or mouse lymphatic endothelial cells (mLECs) compared to mouse hearts injected with control sEVs (pretreated mouse cardiac endothelial cells [mCECs]) or saline. Data are presented as mean ± SEM. *$p < 0.05$, **$p < 0.002$, ***$p < 0.0005$, and ****$p <$

0.0001. *N* = 5–10. Ordinary two-way ANOVA and Tukey's post hoc test were performed among the groups.

(B and C) Histological characterization by Masson's trichrome staining of mouse hearts injected with pretreated CSC^{PDPN+} sEVs or mLECs sEVs showed infiltrative epicardial fibrosis (top) when compared to animals injected with control sEVs or saline (bottom). Scale bar: 0.25 mm.

(D) Fibrotic tissue was characterized by fibronectin deposition (labeled in green; scale bar: 100 μm) and recruited $CD45^{+}$ cells infiltrating the fibrotic tissue (D, bottom, labeled in red and quantified in E; scale bar: 10 μm). Data are presented as mean ± SEM. $*p < 0.05$. *N* = 5–10. Ordinary one-way ANOVA and Tukey's post hoc test were performed among the groups.

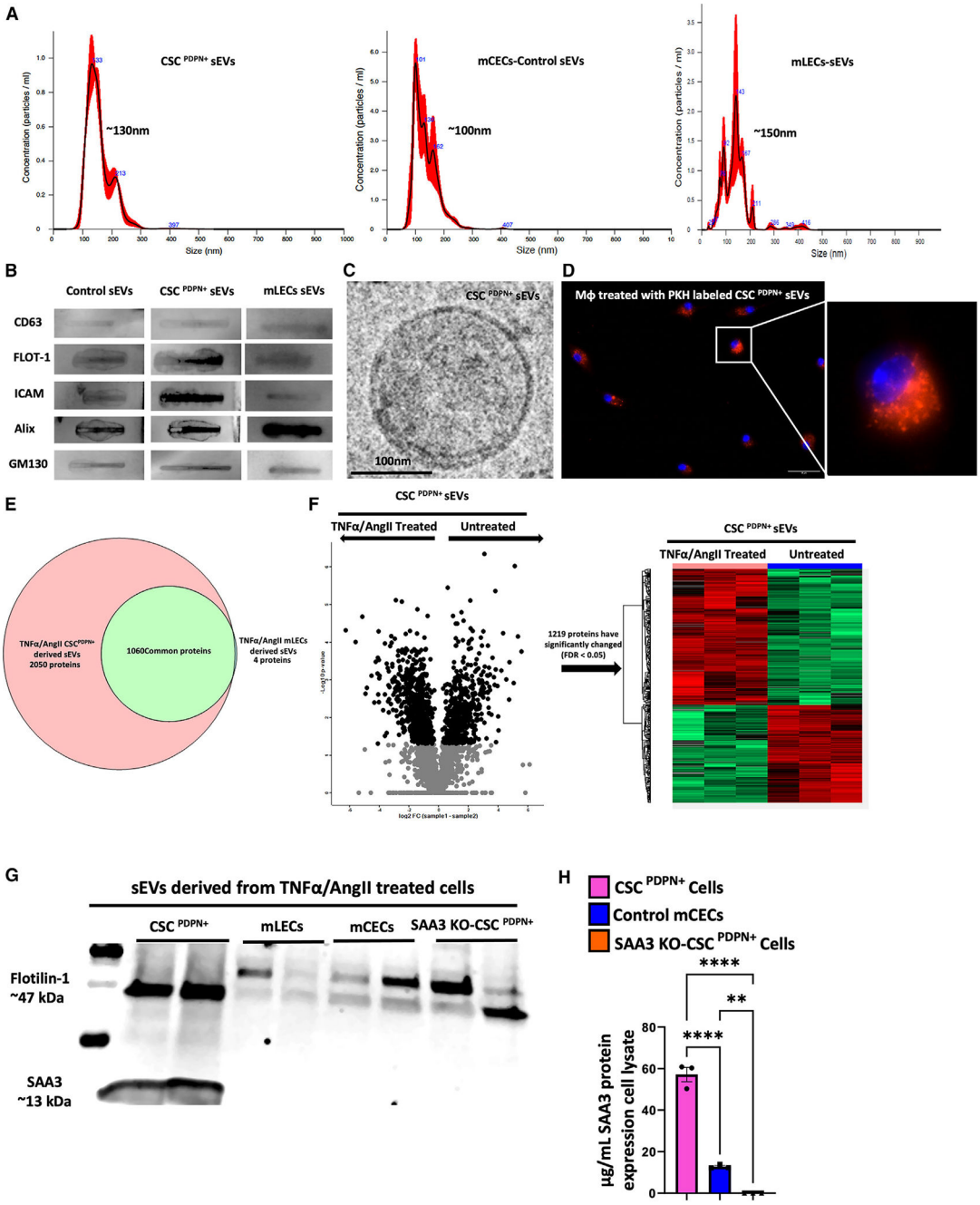

Figure 2. CSC^{PDPN+} sEVs exclusively express SAA3

(A–C) sEVs derived from TNF-α- and AngII-pretreated CSC^{PDPN+}, mLECs, and control mCECs were characterized for size (A) and by sEV protein marker array (B) and transmission electron microscopy (C). Scale bar: 100 nm.

(D) BMDM were treated with PKH 26-labeled (red) CSC^{PDPN+} sEVs to show cell internalization. Scale bar: 25 µm.

(E and F) Mass spectrometry analysis of protein content in sEVs derived from TNF-α- and AngII-pretreated mLECs and CSC^{PDPN+} cells revealed that ~1,000 proteins are commonly

expressed by the two groups of sEVs and that ~2,000 proteins were exclusively expressed in the pretreated CSC^{PDPN+} sEVs (E). Within these 2,000 proteins, ~1,200 were upregulated after TNF-α and AngII treatment, as shown by the volcano plot (F, left) and the heatmap (F, right).

(G) Western blot analysis of isolated sEVs derived from TNF-α- and AngII-pretreated CSC^{PDPN+}, mLECs, mCECs, and SAA3 knockout (KO)-CSC^{PDPN+}.

(H) SAA3 is highly expressed in CSC^{PDPN+} cell lysate after TNF-α and AngII pretreatment. Treatment of mCECs with TNF-α and AngII slightly increased SAA3 expression, which was undetectable in the cells' lysate of CSC^{PDPN+} isolated from global SAA3 KO mice following the same treatment. Data are presented as mean ± SEM. $^{**}p < 0.002$ and $^{****}p < 0.0001$. $N = 3–5$. Ordinary one-way ANOVA and Tukey's post hoc test were performed among the groups.

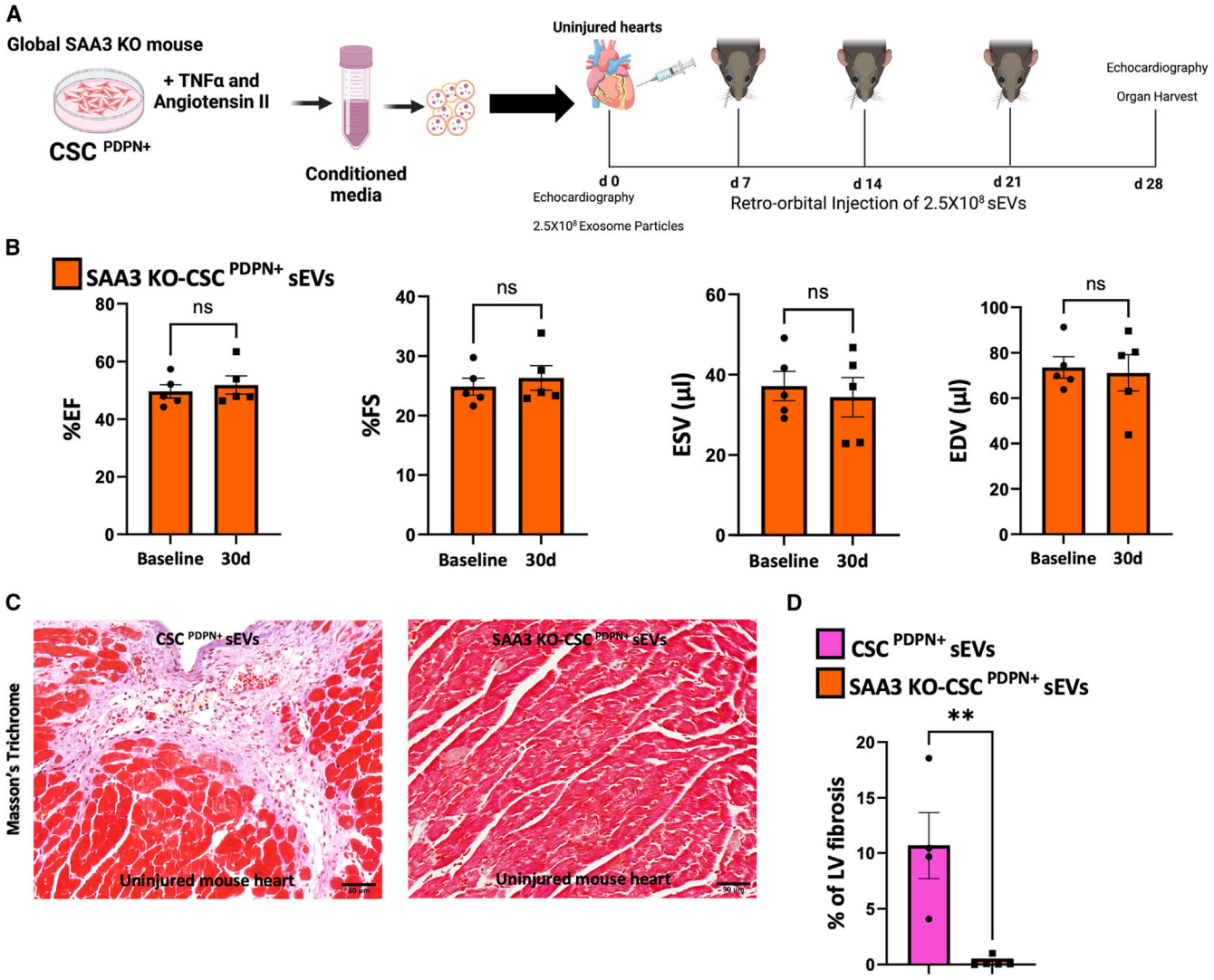

Figure 3. SAA3-KO-CSC^{PDPN+} sEVs did not impair cardiac function in healthy mouse hearts

(A and B) Healthy mouse hearts injected with sEVs isolated from TNF-α- and AngII-pretreated SAA3 KO-CSC^{PDPN+} (A) did not show impairment in heart function during echocardiography analysis (B). Data are presented as mean ± SEM. $N = 5$. Ordinary two-way ANOVA and Tukey's post hoc test were performed among the groups.

(C and D) Treatment of healthy mouse hearts with sEVs isolated from pretreated SAA3 KO-CSC^{PDPN+} failed to induce epicardial and infiltrative fibrosis (C, left) compared to sEVs derived from CSC^{PDPN+} treatment (C, right; quantified in D; scale bar: 50 μm). Data are presented as mean ± SEM. $^{**}p < 0.002$. $N = 5–10$. Student's t test analysis and Tukey's post hoc test were performed between the groups.

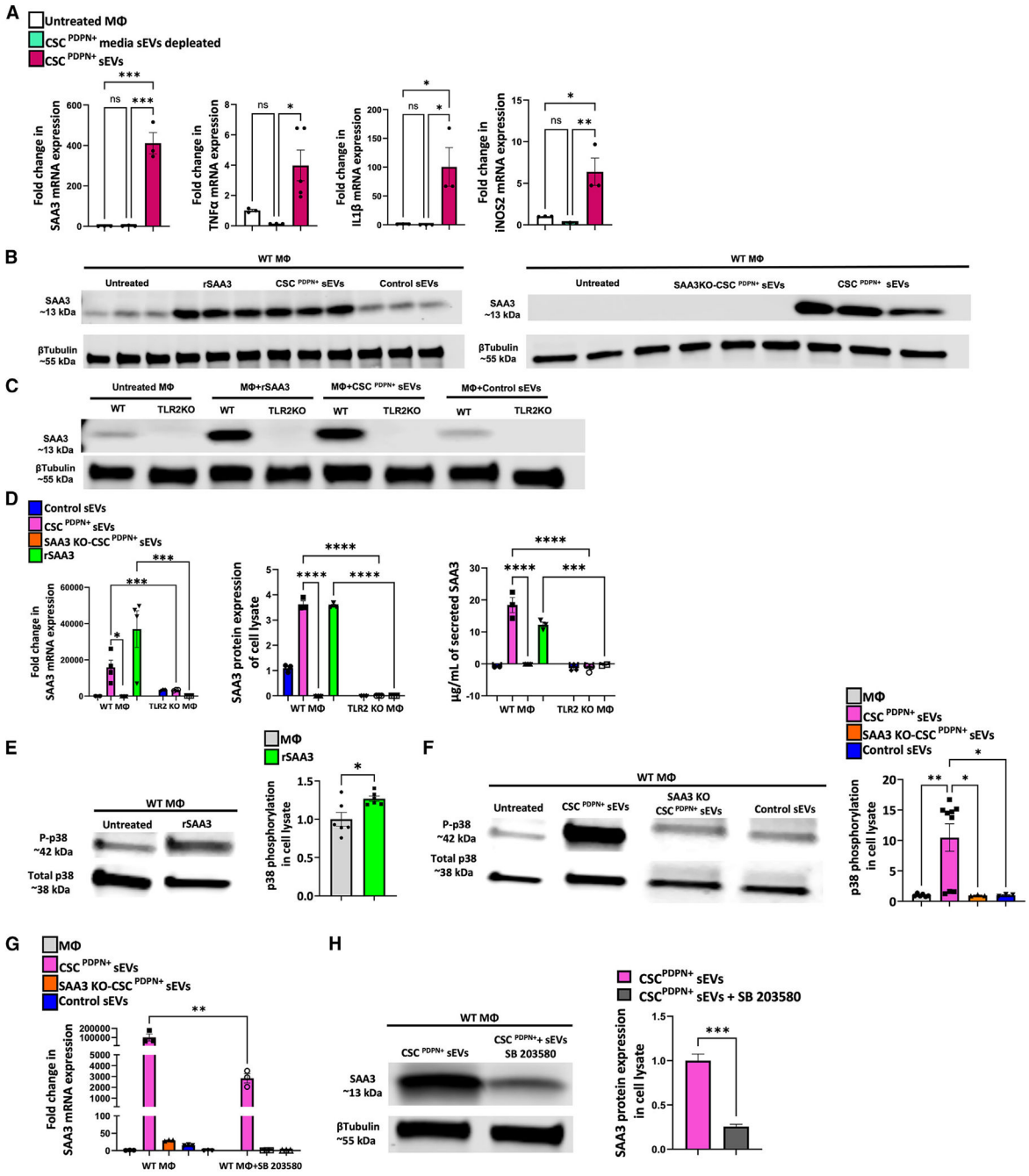

Figure 4. CSC^{PDPN+} sEVs are required to activate and induce SAA3 overexpression in BMDMs via TLR2 activation and p38-MAPK phosphorylation

(A) qPCR analysis of SAA3 and cytokine mRNA in BMDMs (MΦ) stimulated with sEV-depleted CSC^{PDPN+} conditioned medium and with CSC^{PDPN+} sEVs. Data are presented as mean ± SEM. *$p < 0.05$ and ***$p < 0.0005$. $N = 3$. Ordinary one-way ANOVA and Tukey's post hoc test were performed among the groups.

(B) Western blots showing total cell lysate of BMDMs treated either with recombinant SAA3 (rSAA3), sEVs derived from TNF-α- and AngII-pretreated CSC^{PDPN+}, control sEVs derived from similarly treated mCECs, or SAA3-null CSC^{PDPN+}. BMDMs treated

with rSAA3 or CSC^{PDPN+} sEVs specifically expressed SAA3 in cell lysates compared to BMDMs treated with control sEVs.

(C) Western blot showing that BMDMs from TLR2 KO mice did not synthesize SAA3 upon any stimulation.

(D) Quantification of SAA3 expression and release via qPCR, western blot, and ELISA analysis of wild-type and TLR2 KO BMDMs after different treatments. Data are presented as mean ± SEM. *$p < 0.05$, ***$p < 0.0005$, and ****$p < 0.0001$. $N = 3–5$. Ordinary one-way ANOVA and Tukey's post hoc test were performed among the groups.

(E) Western blot analysis and quantification (right) of p38-MAPK phosphorylation (T180/Y182) in BMDMs after treatment with rSAA3.

(F) Western blot analysis and quantification (right) of p38-MAPK phosphorylation (T180/Y182) in BMDMs after treatment with sEVs isolated from TNF-α- and AngII-pretreated CSC^{PDPN+}, sEVs from similarly treated CSC^{PDPN+} from SAA3 KO mice or mCECs. sEVs derived from treated CSC^{PDPN+} from SAA3 KO mice or mCECs only, did not induce p38-MAPK phosphorylation in BMDMs compared to sEVs derived from pretreated CSC^{PDPN+}. Data are presented as mean ± SEM. *$p < 0.05$ and **$p < 0.002$. $N = 3–6$. Student's t test analysis or ordinary one-way ANOVA and Tukey's post hoc test were performed among the groups.

(G) qPCR analysis of SAA3 mRNA in BMDMs shows an important reduction of SAA3 expression after specific inhibition of p38-MAPK with the SB 203580 compound.

(H) Western blot analysis of SAA3 protein expression shows an important reduction of SAA3 synthesis after specific inhibition of p38-MAPK with the SB 203580 compound. Data are presented as mean ± SEM. *$p < 0.05$ and ***$p < 0.0005$. $N = 3–6$. Student's t test analysis or ordinary one-way ANOVA and Tukey's post hoc test were performed among the groups.

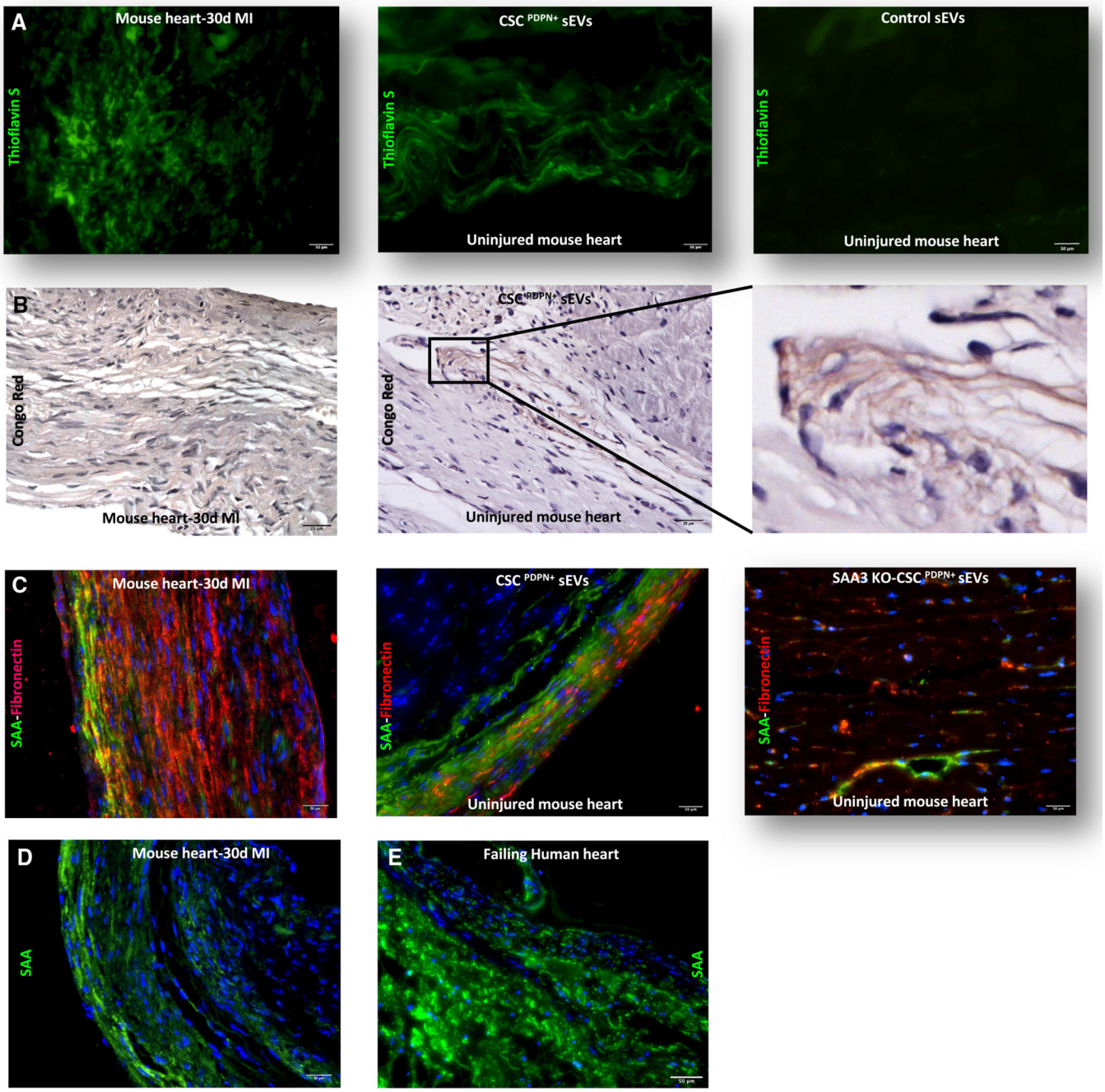

Figure 5. SAA3 aggregates as extracellular amyloid deposits, leading to cardiac amyloidosis

(A and B) Mouse heart sections 30 days after myocardial infarction (MI) (left) and healthy hearts injected with TNF-α- and AngII-pretreated CSC^{PDPN+} sEVs (center) were stained with thioflavin S (scale bar: 50 μm) and Congo red staining (B) (scale bar: 25 μm). Both showed the presence of amyloid deposits when compared with healthy hearts injected with similarly treated mCECs (a right). Congo red staining also showed specific birefringence (B) of amyloid deposits, observed with a polarized light microscope in mouse hearts 30 days after MI or after treatment with CSC^{PDPN+} sEVs.

(C) Immunohistochemistry analysis further showed that SAA, labeled in green, aggregated in ischemic tissue of mouse hearts 30 days after MI along with ECM, labeled with fibronectin in red (left), and sEVs isolated from pretreated CSC^{PDPN+} were able to initiate SAA amyloidosis (center) when injected into healthy mouse hearts (right). Conversely, sEVs derived from pretreated SAA3-null CSC^{PDPN+} failed to induce SAA amyloidosis. Scale bar: 50 μm. $N = 7–10$.

(D and E) Cardiac sections obtained from failing human hearts showed SAA aggregation, labeled in green, in the fibrotic tissue (E) with the same pattern as SAA aggregation in mouse hearts 30 days after MI (D). Scale bar: 50 μm. $N = 7–10$.

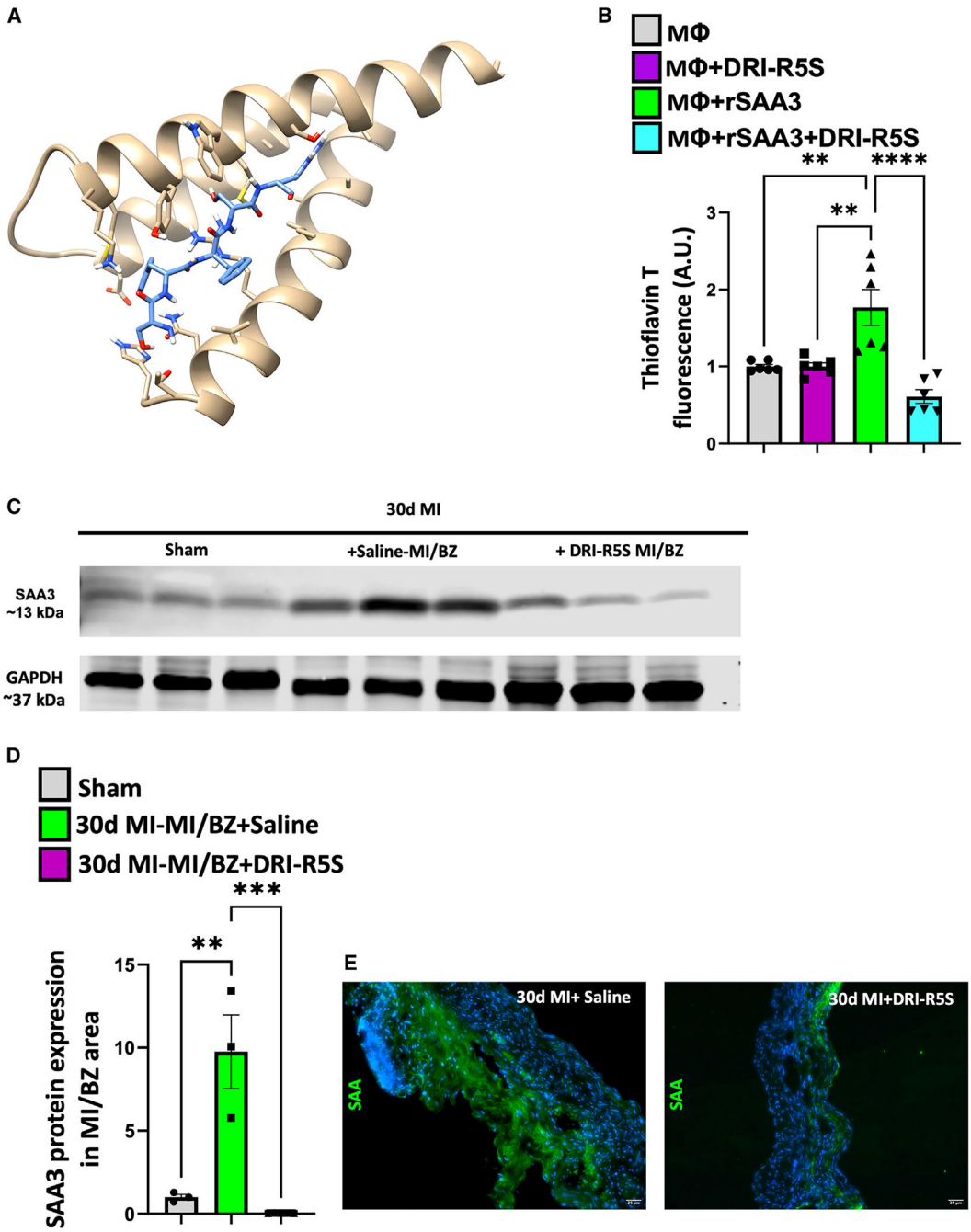

Figure 6. D-Peptide DRI-R5S reduces aggregation of SAA3 *in vivo* and *in vitro*

(A) D-Peptide DRI-R5S docking with the mouse SAA3 motif.

(B) DRI-R5S reduced the aggregation of SAA3 *in vitro* in BMDMs conditioned medium after treatment with rSAA3.

(C and D) *In vivo*, treatment with DRI-R5S reduced the aggregation of SAA3 in the scar border zone area of mouse hearts after MI.

(E) Specific immune-histological staining for SAA showed reduced deposition of SAA in the ischemic area of mouse hearts 30 days after MI when compared with untreated mouse hearts 30 days after MI. Scale bar: 25 μm.

Data are presented as mean ± SEM. $^{**}p < 0.002$, $^{***}p < 0.0005$, and $^{****}p < 0.0001$. $N = 3–5$. Ordinary one-way ANOVA and Tukey's post hoc test were performed among the groups.

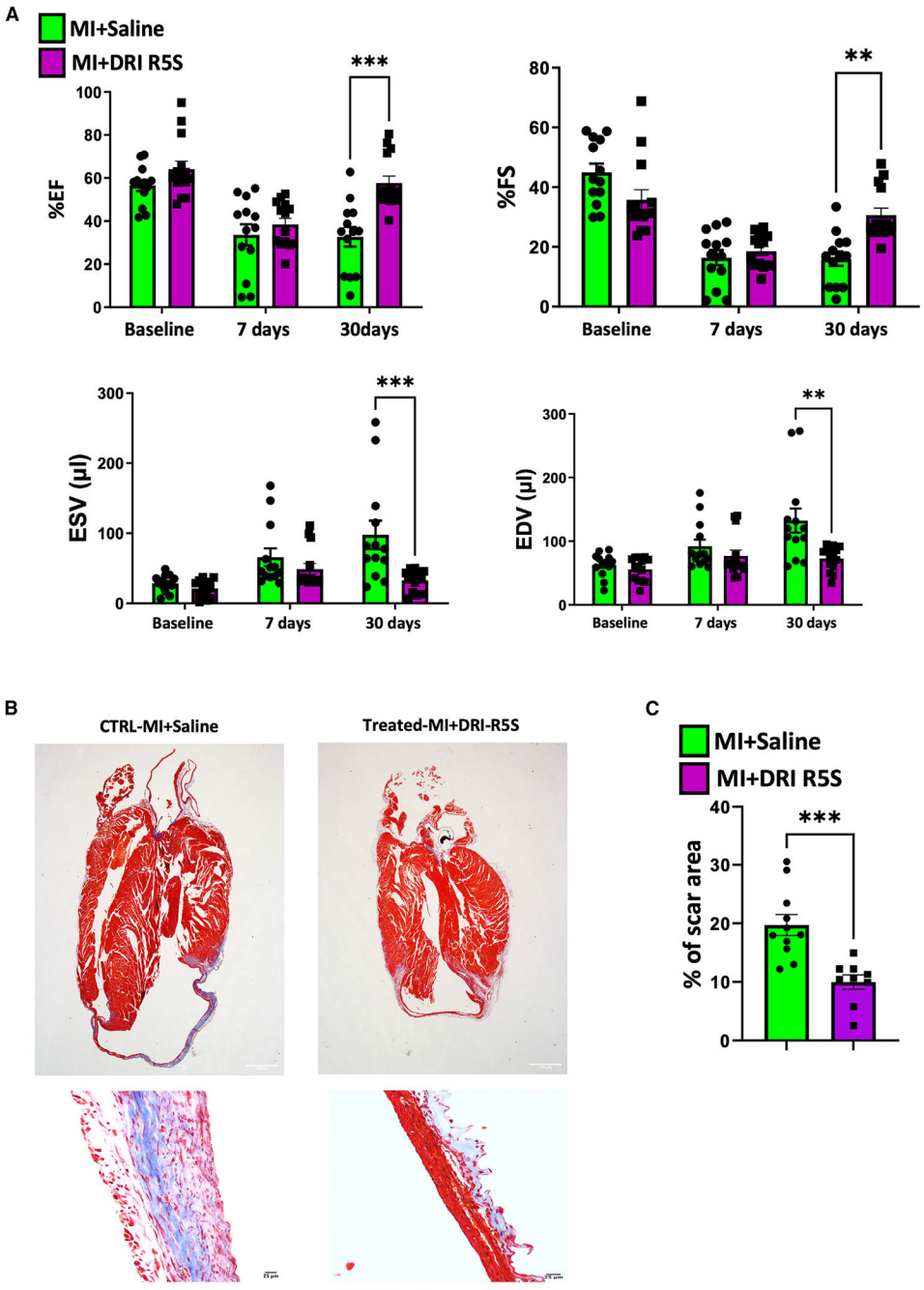

Figure 7. D-Peptide DRI-R5R improves cardiac function after MI

(A) Echocardiographic analysis of wild-type animals that underwent MI and were either treated or not with D-Peptide DRI-R5S. Treated animals showed improved cardiac function. (B and C) Masson's trichrome staining (B) of wild-type animals that underwent MI and were either treated or not with D-Peptide DRI-R5S showed reduced cardiac scar size (C; scale bar: 100 µm) and better left ventricle wall composition (B, magnification; scale bar: 25 µm).

Data are presented as mean ± SEM. *$p < 0.05$, **$p < 0.002$, and ***$p < 0.0005$. $N = 7–10$. Ordinary two-way ANOVA (echocardiography data) or Student's t test analysis and Tukey's post hoc test were performed among the groups.

KEY RESOURCES TABLE

REAGENT or RESOURCE	SOURCE	IDENTIFIER
Antibodies		
Fibronectin	Abcam	Cat# Ab2413
CD45	R&D	Cat# AF114
SAA	Abbexa	Cat# Abx018140
CD31	R&D	Cat# AF3628
Anti-Rabbit 555	Invitrogen	Cat# A31572
Anti-Goat 555	Invitrogen	Cat# A21432
Anti-Mouse 488	Invitrogen	Cat# A21202
SAA3	Abcam	Cat# Ab231680
b-Tubulin	Proteintech	Cat# 66240-1
GAPDH	Proteintech	Cat# 60004-1
Phospho-p38	Cell Signaling Technology	Cat# 28B10
Total-p38	Cell Signaling Technology	Cat# 9212
Anti-Rat (680)	Li-Cor	Cat# 926-68076
Anti-Mouse (800)	Li-Cor	Cat# 926-32212
Anti-Rabbit (800)	Li-Cor	Cat# 926-32213
Anti-Mouse (680)	Li-Cor	Cat# 926-68072
Podoplanin	R&D	Cat# BAF3244
Lyve-1	Abcam	Cat# Ab14917
CD68	Abcam	Cat# Ab31630
Chemicals, peptides, and recombinant proteins		
Lysis buffer	Cell Signaling Technology	9803S
Complete Mini Proteinase inhibitor cocktail	Roch	11836153001
Halt Phosphatase Inhibitor cocktail	Thermo Scientific	1862495
Quiazol	Qiagen	1038703
Masson Trichrome staining	Sigma-Aldrich	HT15-1KT
Bouin’s solution	Sigma-Aldrich	HT101128-4L
Congo red staining	Sigma-Aldrich	HT60-1KT
Thioflavin S	Acros Organics	2390-54-7
Thioflavin T	Thermo Scientific	1326-12-1
Collagenase type 2	Worthington Biochemical Corp.	LS004176
Anti-Biotin Microbeads	Milteniy	130-090-485
Collagen	Sigma-Aldrich	5074
EDTA	Sigma	E8008
Histopaque	Sigma-Aldrich	10831-100ML
Dulbecco’s Modified Eagle’s Medium/Nutrient Mixture F-12 Ham	Corning	10-092-CV
Dulbecco’s Modified Eagle’s Medium	Corning	10-013-CV

REAGENT or RESOURCE	SOURCE	IDENTIFIER
RPMI Medium 1640	Gibco	22400-089
EBM-2	Lonza	CC-3156
EGM-2 Single Quots	Lonza	CC-4176
ECGS endothelial cell growth supplement	Abd Serotec	4110-5004
HEPES	Gibco	15630-080
mCECs	Cedarlane	CLU510
L929	ATCC	30-2003
Macrophage colony-stimulating factor	Sigma-Aldrich	M-917010UG
DRI-R5S (sequence from N terminus to C terminus is SFFSR)	Synthesized by Biomatik	N/A
TNF-alpha, mouse, recombinant	R&D System	aa 80-235
Angiotensin II	Sigma	A9525-1MG
Recombinant SAA3	Biomatik	RPC20262
LPS	Sigma-Aldrich	L4391-1MG
SB 203580	Cayman Chemical Company	13067
Intercept Blocking Reagent	LI-COR	927-70001
PKH26	Sigma-Aldrich	MINI26-1KT
DAPI (4′,6-diamidino-2-phenylindole dihydrochloride)	Sigma-Aldrich	D9542
Critical commercial assays		
Mouse SAA3 ELISA kit	Millipore	EZMSAA3-12K
Mouse Exo-Check™ Exosomes Antibody Array	System Biosciences, Palo Alto, CA	EXORAY400A-4
92-plex discovery assay	RayBiotech	S061008
SAA3 ELISA kit	Eve Technologies	EZMSAA3-12K
Pierce BCA protein assay kit	Thermo Scientific	23225
miRNeasy Mini Kit	Qiagen	1038703
cDNA revere transcription kit	Applied Biosystems	43688114
Fast SYBR Green Master Mix	Applied Biosystems	4385612
Deposited data		
Single cell seq	Source: Forte et al.[53]	Array Express: E-MTAB-7895
Proteomics	EV Mass spectrometry	MassIVE MSV000097049
Experimental models: Organisms/strains		
Ten to twelve-week-old male mice (C57BL/6J)	Jackson Research Laboratory, Bar Harbor, ME	000664
Ten to twelve-week-old male mice Toll Like Receptor 2 knockout (TLR2KO; Jackson Labs; Tlr2tm1Kir/J)	Jackson Research Laboratory, Bar Harbor, ME	004650
Ten to twelve-week-old male mice Serum Amyloid A3 (SAA3) (Jackson Labs; Del(7Saa3-Saa2)738Lvh/J) knockout mice (SAA3 KO)	Jackson Research Laboratory, Bar Harbor, ME	034856
Oligonucleotides		
Mouse SAA3	See Table S3	IDT
Mouse TNFα	See Table S3	IDT

REAGENT or RESOURCE	SOURCE	IDENTIFIER
Mouse IL-1β	See Table S3	IDT
Mouse iNOS2	See Table S3	IDT
Mouse PDPN	See Table S3	IDT
Software and algorithms		
GraphPad Prism 9	GraphPad Prism Software, Inc	https://www.graphpad.com
Vevo 2100 Imaging System	Fujifilm Visualsonics	https://www.visualsonics.com
VevoLAB 5.8.1 software imaging system	Fujifilm Visualsonics	https://www.visualsonics.com/
Vevo strain function of VevoLAB 5.8.1 software imaging system	Fujifilm Visualsonics	https://www.visualsonics.com
Jenoptik Graphax® Kapella	Jenoptik	https://www.jenoptik.us
Bioquant, Life Science 2022 software version, Nashville, TN	Bioquant	https://community.bioquant.com
Adobe Photoshop (Adobe) software	Adobe	https://www.adobe.com
ImageJ 1.52h	National Institute of Health	https://imagej.nih.gov/
Odyssey® CLx Imaging System	Biotecne	https://www.bio-techne.com
Image Studio™ Lite Software	LI-COR	https://www.licorbio.com
HADDOCK	HADDOCK	https://rascar.science.uu.nl/haddock2.4/
PRODIGY	PRODIGY	https://rascar.science.uu.nl/prodigy/